# S/WAVES: The Radio and Plasma Wave Investigation on the STEREO Mission

J.L. Bougeret · K. Goetz · M.L. Kaiser · S.D. Bale · P.J. Kellogg · M. Maksimovic ·
N. Monge · S.J. Monson · P.L. Astier · S. Davy · M. Dekkali · J.J. Hinze ·
R.E. Manning · E. Aguilar-Rodriguez · X. Bonnin · C. Briand · I.H. Cairns ·
C.A. Cattell · B. Cecconi · J. Eastwood · R.E. Ergun · J. Fainberg · S. Hoang ·
K.E.J. Huttunen · S. Krucker · A. Lecacheux · R.J. MacDowall · W. Macher ·
A. Mangeney · C.A. Meetre · X. Moussas · Q.N. Nguyen · T.H. Oswald · M. Pulupa ·
M.J. Reiner · P.A. Robinson · H. Rucker · C. Salem · O. Santolik · J.M. Silvis ·
R. Ullrich · P. Zarka · I. Zouganelis

J.L. Bougeret · M. Maksimovic (✉) · N. Monge · P.L. Astier · S. Davy · M. Dekkali ·
R.E. Manning (deceased in 2002) · X. Bonnin · C. Briand · B. Cecconi · S. Hoang · A. Lecacheux ·
A. Mangeney · Q.N. Nguyen · P. Zarka · I. Zouganelis
LESIA, UMR CNRS 8109, Observatoire de Paris, 92195 Meudon, France
e-mail: milan.maksimovic@obspm.fr

K. Goetz · P.J. Kellogg · S.J. Monson · J.J. Hinze · C.A. Cattell · J.M. Silvis
School of Physics and Astronomy, University of Minnesota, Minneapolis, USA

M.L. Kaiser · J. Fainberg · R.J. MacDowall · C.A. Meetre · M.J. Reiner
NASA, Goddard Space Flight Center, Greenbelt, MD, USA

S.D. Bale · E. Aguilar-Rodriguez · J. Eastwood · K.E.J. Huttunen · S. Krucker · M. Pulupa · C. Salem ·
R. Ullrich
Space Sciences Laboratory, University of California, Berkeley, USA

S.D. Bale · M. Pulupa
Physics Department, University of California, Berkeley, USA

I.H. Cairns · P.A. Robinson
School of Physics, University of Sydney, Sydney, NSW 2006, Australia

R.E. Ergun
Laboratory for Atmospheric and Space Physics, University of Colorado, Boulder, USA

W. Macher · T.H. Oswald · H. Rucker
Space Research Institute, Austrian Academy of Sciences, Graz, Austria

X. Moussas
Section of Astrophysics, Astronomy and Mechanics, Department of Physics, University of Athens,
Athens, Greece

M.J. Reiner
The Catholic University of America, Washington, DC, USA

**Abstract** This paper introduces and describes the radio and plasma wave investigation on the STEREO Mission: STEREO/WAVES or S/WAVES. The S/WAVES instrument includes a suite of state-of-the-art experiments that provide comprehensive measurements of the three components of the fluctuating electric field from a fraction of a hertz up to 16 MHz, plus a single frequency channel near 30 MHz. The instrument has a direction finding or goniopolarimetry capability to perform 3D localization and tracking of radio emissions associated with streams of energetic electrons and shock waves associated with Coronal Mass Ejections (CMEs). The scientific objectives include: (i) remote observation and measurement of radio waves excited by energetic particles throughout the 3D heliosphere that are associated with the CMEs and with solar flare phenomena, and (ii) in-situ measurement of the properties of CMEs and interplanetary shocks, such as their electron density and temperature and the associated plasma waves near 1 Astronomical Unit (AU). Two companion papers provide details on specific aspects of the S/WAVES instrument, namely the electric antenna system (Bale et al., Space Sci. Rev., 2007) and the direction finding technique (Cecconi et al., Space Sci. Rev., 2007).

**Keywords** Solar radioastronomy · Space instrumentation

# 1 Introduction

The measurement of fluctuating electric fields at a spacecraft in interplanetary space using simple monopole or dipole antenna systems gives access to both remotely produced electromagnetic waves (radio astronomy) as well as electromagnetic and electrostatic waves produced in the vicinity of the spacecraft.

Long wavelength radio astronomy covers the range of decametric, hectometric and kilometric wavelengths (or radio frequencies below roughly 30 MHz), which are usually not well detected from ground-based radio observatories without perturbations due to the reflection of radiation from Earth's ionosphere. At these wavelengths, a rich variety of radio bursts of solar origin are observed that trace particles produced by energetic phenomena through the solar corona and interplanetary medium. Since the late 1960's, these radio emissions have been observed and studied, primarily by numerous single spacecraft missions. These radio emissions are produced by non-thermal radiation mechanisms that are still incompletely understood. The STEREO mission will provide the first dedicated stereoscopic observations of remotely generated solar radio emissions to elucidate their origin.

In-situ observation of waves can yield valuable information on processes occurring throughout the heliosphere. Of special importance are processes which include the generation of radio waves, cascade of plasma turbulence, reconnection at flux-tube boundaries, etcetera.

The accurate measurement of the weak noise spectrum near the local plasma frequency (plasma line) can yield a robust measurement of the electron density and temperature, e.g., when a Coronal Mass Ejection (hereafter CME) crosses the spacecraft. This measurement

O. Santolik
Faculty of Mathematics and Physics, Charles University, Prague, Czech Republic

O. Santolik
IAP/CAS, Prague, Czech Republic

technique, called Quasi-thermal noise spectroscopy (Meyer-Vernet and Perche 1989), is independent of the spacecraft potential even when the spacecraft environment is disturbed by the passage of a CME.

Radio and plasma wave investigations are currently part of the payload of several spacecraft in the earth environment and of interplanetary or planetary probes. They provide unique information that is complementary to particle and other in-situ measurements. In particular, the Ulysses, WIND, and CASSINI spacecraft are carrying similar instruments, portions of which have been designed and built by the same institutions as S/WAVES (Stone et al. 1992; Bougeret et al. 1995; Gurnett et al. 2004). Both Ulysses and WIND are spinning spacecraft, while CASSINI and STEREO are three-axis stabilized. The instruments on the latter two spacecraft use similar techniques to determine source direction, though the S/WAVES measurement techniques are more sophisticated. These methods of analysis are described in more detail in a companion paper devoted to direction finding of radio sources from three-axis stabilized spacecraft, such as STEREO (Cecconi et al. 2007). The STEREO antenna system used for making these measurements is described in the companion paper by Bale et al. (2007). The implications of these radio and plasma wave measurements for theoretical studies and modeling are summarized in the paper by Aschwanden et al. (2006).

In Sect. 2, we summarize the S/WAVES scientific objectives and provide the scientific background relevant for the radio stereoscopic observations that will be made during the STEREO mission. In Sect. 3, we give a brief summary of the direction-finding method as well as the quasi-thermal noise spectroscopy method. The S/WAVES suite of instruments is described in detail in Sect. 4 and specific technical aspects, including Electro-Magnetic Cleanliness, inter-communication with other STEREO instruments and calibration, are presented in Sect. 5. Scientific operations are outlined in Sect. 6 and the Education and Public Outreach plan is summarized in Sect. 7. Finally, Sect. 8 provides an overall summary and conclusion.

## 2 Scientific Objectives

### 2.1 Summary of S/WAVES Science Objectivs

The primary S/WAVES science goals are to:

– Remotely track and probe CME-driven shocks and flare electrons at high frequency and time resolution from their genesis in the low corona to their interaction with the terrestrial magnetosphere, to establish the link between the EUV and coronagraph images and the in-situ CME and particle observations.
– Measure the spatial extent and structure of CME-driven shocks and flare- and CME-associated electron beams.
– Make remote and in-situ measurements of solar radio sources that may provide a deeper and more comprehensive understanding of the mechanisms that generate type II (CME) and type III (flare) radio bursts.
– Measure solar wind electron plasma density and temperature in regions of cold, dense plasma within CME-associated magnetic clouds using quasi-thermal noise techniques.
– Study the role of plasma microphysics in CME-driven shocks.

## 2.2 Remote Sensing of Type II (CME-Associated) and Type III (Flare-Associated) Solar Radio Emissions

CMEs, once ejected from the Sun (after, for example, large filament eruptions) propagate through the corona and interplanetary medium. When directed towards the Earth, they can affect the space weather environment in two ways: by accelerating solar energetic particles (SEPs) near the Sun and later by the direct encounter of the CME material and its associated driven shock with the Earth's magnetosphere. Since radio emissions are often generated at CME-driven shocks, these radio observations provide an important means of tracking CMEs through the corona and the interplanetary medium, a crucial capability for space weather forecasting, as discussed in Sect. 6.2 (Gopalswamy et al. 2001b; Schwenn et al. 2005).

Radio emissions associated with the propagation of a CME are called *type II radio bursts or emissions*. The mechanism responsible for the generation of these radio emissions at the fundamental and harmonic of the local plasma frequency and the relevant in-situ observations are described in Sects. 2.3 and 2.4. Because the interplanetary density decreases with increasing heliocentric distance, the type II emissions decrease in frequency as the CME/shock propagates through the corona and the interplanetary medium. An example of such frequency drift is shown on the dynamic spectrum of Fig. 1a.

Remote measurements of the frequency drift of these type II emissions provide a frequency-time track of the CME/shock through interplanetary space. In the example displayed in Fig. 1, which was an Earth-directed (halo) CME event, the diffuse radio emissions were continuously observed as the CME propagated from the solar corona to Earth. Once a heliospheric density model is assumed, this frequency-time track can be converted
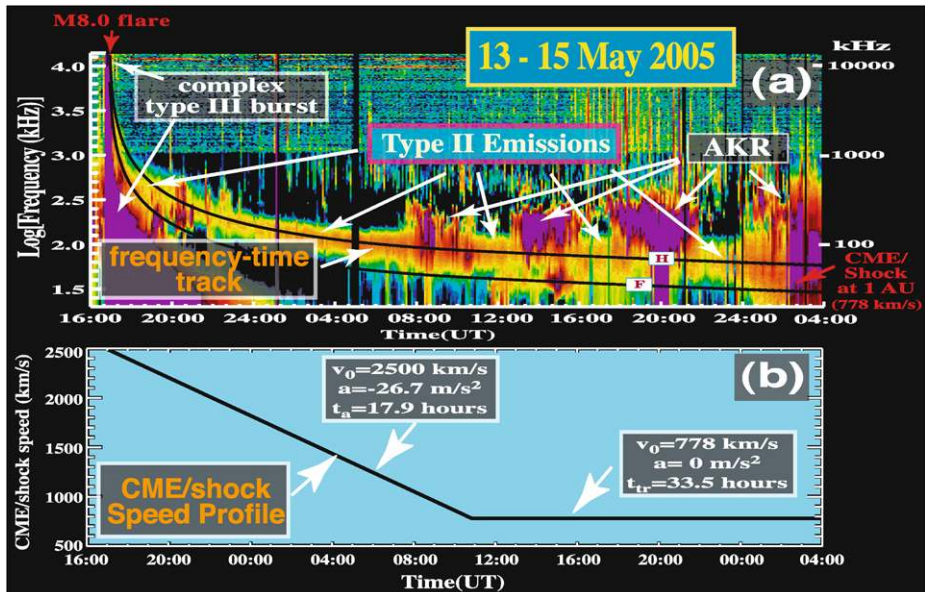


**Fig. 1** (**a**) Dynamic spectrum from WIND/WAVES showing the frequency-drifting type II radio emissions generated by a halo CME as it propagated from the Sun to Earth between May 13 and 15, 2005. The *black curves* are the frequency–time tracks of the frequency-drifting type II radiation, generated at the fundamental and harmonic of the plasma frequency. (**b**) Speed profile of the corresponding CME derived from the frequency–time track in (**a**), assuming a $1/r^2$ falloff of the interplanetary plasma density

into a distance–time track that describes the spatial progress of the propagating CME. The CME/shock speed profile, such as shown in Fig. 1b, can then be derived directly from this distance-time track, showing that the CME initially decelerated at a rate of 27 m/s$^2$ in this particular case.

Until the recent advent of heliospheric imagers, this model-dependent approach has been the most efficient way for indirectly tracking CMEs. This method has been used to reconstruct the speed and distance-time profiles describing the spatial progress of CMEs through interplanetary space (Reiner et al. 1998a, 2001a, 2007b; Dulk et al. 1999). On STEREO, such remote radio observations will provide overlapping coverage with the SECCHI white-light images of CMEs, including in the critical spatial region between 60 and 100 solar radii (Rs) where significant changes in CME dynamics are expected as the CME moves from the solar corona to the interplanetary solar wind.

A shortcoming of remote frequency–time tracking is that the coronal and interplanetary density profiles, required to convert to spatial information, are dynamic and typically not known *a priori*. S/WAVES, however, can overcome this difficulty by exploiting the direction finding capabilities on both spacecraft. The 3D spatial location of a given radio source can be directly deduced using radio triangulation, i.e. from the intersection of the measured lines of sight from the two STEREO spacecraft, without any assumptions for the interplanetary density profile (see Sects. 3.3 and 3.4 for details). The two spacecraft triangulations, measured at a series of consecutive frequencies, allow direct spatial tracking of a given solar radio source and, in the case of a type II burst, of the associated CME/shock.

Comparison of the 3D locations of the radio sources with the corresponding white-light CME, provided by SECCHI on STEREO (Howard et al. 2008) and SOHO LASCO (Brueckner et al. 1995), will provide new information about the spatial relationship between the CME and its associated driven shock, and about conditions favorable to the generation of these radio emissions (Reiner et al. 1998b, 2005).

The S/WAVES radio observations will provide a better understanding of the complex features commonly observed for type II radio emissions. In addition to the more continuous and diffuse emissions shown in Fig. 1, type II radiation consisting of intermittent, narrow bands of emissions that can often be nearly as intense as the radiation from solar type III emissions, have often been reported. Some of the intense, complex type II emission features represent signatures of interactions between two propagating CMEs (Gopalswamy et al. 2001a; Reiner et al. 2001b). An example of enhanced radio emissions resulting from such interactions is shown in Fig. 2. The ability of S/WAVES to view these emissions from two vantage points and to triangulate the actual radio source spatial locations, which can then be directly compared with the stereo views of the associated white-light CME, will provide a better understanding of the origin and nature of these unusual type II radiation features. Analysis of the STEREO observations will also provide important new information on the beaming patterns of the type II emissions and on the propagation characteristics of radiation through the interplanetary plasma. The analysis and interpretation of these observations will be greatly facilitated by complementary modeling efforts (Knock and Cairns 2005; Aschwanden et al. 2006). Finally, these STEREO observations of the type II radio signatures may provide new insights into the origin and nature of solar energetic particles (SEPs) (Gopalswamy et al. 2002, 2005).

Although the same plasma emission mechanism that generates type II radio emissions also generates type III radio bursts, the origin of these latter bursts is quite different. Type III radio bursts are produced by streams of suprathermal electrons ejected onto open magnetic field lines during solar flares. These electrons, due to their small gyroradii, are constrained to follow the Parker spiral magnetic field lines through interplanetary space, generating intense
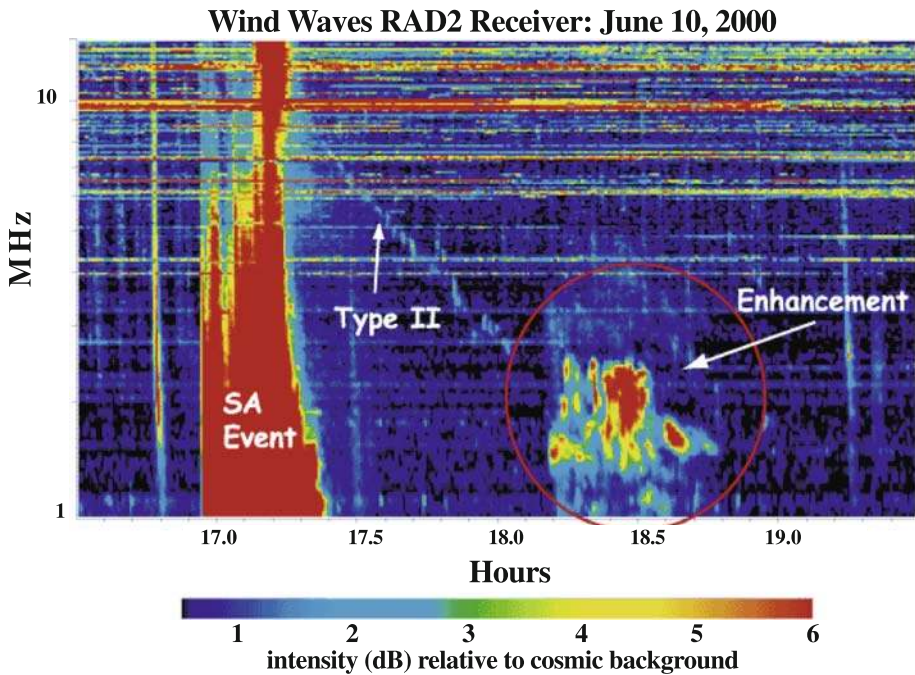
**Fig. 2** Enhanced type II radiation due to the interactions between two CMEs

**Fig. 3** (Color online) Stereo image of a type III burst trajectory deduced by triangulation from the WIND and Ulysses spacecraft for a solar type III event observed on May 20, 2001 at about 06:40 UT. The *yellow dashed lines* are the lines of sight to the radio source from the Ulysses and WIND spacecraft, whose intersection gives the 3D location of the radio source at each observing frequency. (To view the 3D stereo image, relax the eyes (by focusing at a distant object through the page) and allow the two images to merge into a third image at the center of the page, which will be seen in 3D)
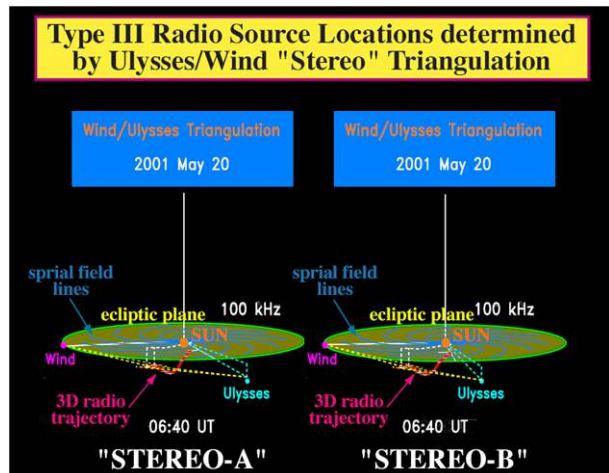


radio emissions with their passage. The locations of the radio sources for the type III bursts at different frequencies, therefore, trace the global structure of the interplanetary magnetic field. An example of a 3D trajectory obtained from two spacecraft triangulation for a type III radio burst is shown in Fig. 3.

The orbital geometry of STEREO is ideal for routinely performing such triangulation measurements. The triangulation is expected to work best when the angular separation of the STEREO spacecraft is between about 40 and 60 degrees. The stereo views, as shown in Fig. 3, provide an opportunity to measure the beaming patterns of the type III radiation, to deduce the intrinsic characteristics of the type III radio sources and to study the effects of propagation and scattering of the radiation in the interplanetary medium (Hoang et al. 1997; Reiner et al. 1998c). These observations are important for providing a deeper understanding of the emission mechanism, as discussed in Sect. 2.4.

STEREO/WAVES observations will also provide a new understanding of the *complex type III-like bursts* (formerly called SA events) that are nearly always associated with major flare events involving CMEs (Cane et al. 1981; Bougeret et al. 1998; Reiner et al. 2000). Reiner and Kaiser (1999) pointed out the unusual fine-structure characteristics of these complex type III-like emissions below about 10 MHz, such as shown in Figs. 1 and 2. The STEREO observations, performed simultaneously from different spatial viewpoints, will give a better understanding of the nature and origin of these unusual radiation characteristics.

Solar *type III radio storms*, which originate in quasi-stable active regions, are long-lasting, quasi-continuous events consisting of thousands of weak type III radio bursts per day. Single spacecraft observations of these type III storms have used dynamic parallax to deduce the 3D locations of the radio sources (Bougeret et al. 1984). STEREO independently determines the source locations with two spacecraft triangulation. Information on the propagation and scattering effects of the interplanetary plasma on the type III radiation are obtained from the comparison of the type III source locations using these two complementary techniques. It has recently been discovered that type III radio storms are weakly circularly polarized (Reiner et al. 2007a). These observations were used to deduce the radial dependence of the solar magnetic fields along the path of electron beams. By simultaneously providing the corresponding 3D beam trajectory, the STEREO observations may identify the interplanetary plasma structure associated with the magnetic field profile by revealing the corresponding density profile.

## 2.3 Observation of In-Situ Type II and III Source Regions

As discussed above, type II and type III radio bursts are generated by the "plasma" emission process. As shock- or flare-accelerated energetic electrons propagate in the interplanetary medium, they form beam-like (positive slope) features in phase space. These beams are thought to form by simple advection, the fast electrons running ahead of the slower ones. As this beam feature moves toward lower energies, it becomes more and more "dense" until the growth rate, which is related to the positive slope of the electron distribution function, is sufficient to excite Langmuir waves. Eventually, the beam feature falls below the solar wind thermal/suprathermal electron population. Electrons with energies between ∼1–10 keV are thought to be responsible for generating the Langmuir waves, which eventually couple to propagating electromagnetic radiation. This region of unstable electron beams and Langmuir wave growth is often called the "source region" of the radio burst.

The theoretical understanding of the radiation from beams of suprathermal electrons in the solar atmosphere is based on comprehensive observations from space including both radio and in-situ observations and on energetic particle and plasma measurements (Lin et al. 1981; Robinson et al. 1993; Cairns and Robinson 1997, 1998, 1999). Type III source regions were encountered by the ISEE-3 (for, e.g., Lin et al. 1981) and WIND (for, e.g., Ergun et al. 1998) spacecraft. These earlier studies have left several questions unanswered:

(1) What is the mechanism of coupling between Langmuir waves and radio waves?
(2) How does the electron beam remain "unstable" over 1 AU of transit?
(3) What are the spatial dimensions of the source and the fraction of the source volume actually emitting radiation (the so-called filling factor)?
(4) What is the role of density fluctuations in the radio emission process?

S/WAVES observations, with 3-axis wave measurements, will allow us to take the next step in addressing these questions. The S/WAVES Time Domain Sampler (TDS) will measure the polarization state of Langmuir waves, their location within density structures (with the Low Rate Science (LRS) and Antenna Potential Monitor (APM) measurements), and their statistical properties (with the Langmuir Wave Statistics (LWS) measurements). Coordination with the IMPACT/STE instrument on STEREO (Luhmann et al. 2007) will provide important new measurements of the properties of electron beams associated with waves. In addition, combined with WIND (Bougeret et al. 1995) and ACE (Stone et al. 1998 and references therein) measurements, STEREO may provide the first spatial measurements of the source region. In its first month in orbit, STEREO has already observed at least one in-situ type III burst.

Type II radio bursts are generated upstream of fast CME-driven IP shocks. The radio emission process is fundamentally the same as for type III bursts, but beam speeds are probably lower (500 eV–1.5 keV). Type II bursts are often observed to be patchy in nature, with radio emission apparently coming from multiple sites near the shock front. However, only a few type II radio sources have been observed in-situ (Bale et al. 1999; Pulupa and Bale 2006). The first published event (Bale et al. 1999) showed a highly structured shock with radio emission coming from within a "bay" on the shock front. The STEREO spacecraft, together with WIND and ACE, will allow for the first multi-spacecraft studies of in-situ type II bursts.

## 2.4 Contribution of STEREO to the Theory of Radio Emission in the Interplanetary Medium

The STEREO data will constrain theories for interplanetary radio emissions using both remote observations (Aschwanden et al. 2006) and in-situ detection of plasma waves, density fluctuations, particle distributions, shock waves and other source characteristics responsible for producing the radiation. One unique aspect is the ability of S/WAVES to triangulate remote radio sources with near simultaneous Low Frequency Receiver (LFR), High Frequency Receiver (HFR) and Fixed Frequency Receiver (FFR) data from both STEREO spacecraft.

In the past decade or so, the theory of radio wave generation set out by Ginzberg and Zheleznyakov (1958), as modified by Melrose (1982), Cairns (1988) and others, has been challenged by several different mechanism. The original theory treated the conversion of electrostatic waves to electromagnetic waves by scattering from electron polarization clouds around ions, while the modified theory involves decay processes involving ion acoustic waves (Melrose 1982; Cairns 1988; Robinson and Cairns 1998a). Alternatively Kellogg (1986) pointed out that the Langmuir waves should be subject to reflection and trapping by density fluctuations, providing an alternative source of scattered Langmuir waves than nonlinear processes. Finally, Field (1956) introduced the idea that conversion of electrostatic waves could take place at major density gradients, and more recently, a series of papers have considered this process for the strong density fluctuations in the solar wind (Hinkel-Lipsker et al. 1992; Yin et al. 1999; Willes and Cairns 2001). The simultaneous detection of three-axis electric waveforms of Langmuir waves and low frequency fluctuations using the Time

Domain Sampler (TDS) and Low-Rate Science (LRS) experiments will provide constraints on these processes, as described in the subsections below.

### 2.4.1 Low Frequency Receiver (*LFR*), High Frequency Receiver (*HFR*) and FFR Receiver Science

S/WAVES is expected to make four primary contributions to the theory of type II and III bursts using remote observations:

(1) S/WAVES will use LFR, HFR and FFR data to test theoretical predictions for the dynamic spectra, fluxes, brightness temperatures, polarization and time-varying source locations of type II and III bursts. Increasingly sophisticated theories (Robinson and Cairns 1998a, 1998b; Knock and Cairns 2005; Cairns and Knock 2006; Aschwanden et al. 2006) were motivated by the anticipated solar wind data available from STEREO/IMPACT, S/WAVES thermal noise spectroscopy (Sect. 3.5), and other spacecraft.

(2) FFR, LFR and FFR direction finding and triangulation analyses, combined with theory-data comparisons, will allow the role of scattering by density irregularities to be disentangled from intrinsic directivity patterns (Steinberg et al. 1984; Thejappa and MacDowall 2005). Establishing whether the directions and source sizes inferred from each spacecraft's data independently are consistent with the triangulation solution and correlating 3D information on the source (e.g., location, size, and time variations) are key to this analysis.

(3) The relationship of burst "hotspots" to CMEs, shocks, interactions between several CMEs and solar wind structures (cf. Reiner et al. 1998a; Gopalswamy et al. 2001a; Knock and Cairns 2005) will be firmly established and quantified using S/WAVES direction-finding capabilities and data-driven solar wind models and will provide a means of testing current theories on the relationship.

(4) Radio sources like Earth's auroral kilometric radiation (AKR) and similar radiation from Jupiter and Saturn, which have known locations and independently measured spectra and intensity, will undergo changes in direction, angular size and intensity that provide independent constraints on scattering by density irregularities (Hess and MacDowall 2003) along multiple lines of sight to the two STEREO spacecraft, both in heliocentric longitude (for Earth) and distance (for Jupiter and Saturn).

### 2.4.2 Time Domain Sampler (*TDS*)

TDS observations of local Langmuir waves in type II and III events and comparisons with associated IMPACT and PLASTIC data will strongly constrain theories for type II and III bursts. Three major coupled questions need to be answered (Cairns and Kaiser 2002; Kellogg 2003): (i) why are the waves bursty, (ii) what is the origin of the localized wave packets that are sometimes observed, and (iii) what are the roles of linear and nonlinear processes in the evolution of Langmuir waves and the production of type II and III radiation?

In addition to these major studies, simultaneous high time resolution ($\approx 1$ µs) TDS data on 3 electric antennas will allow detailed comparison with stochastic growth theory (SGT) (Robinson 1992, 1995; Robinson et al. 1993; Cairns and Robinson 1999; Robinson and Cairns 2001), together with frequency-domain and correlation analyses of nonlinear product waves (Bale et al. 1998), and investigation of the reflection and linear mode conversion of Langmuir waves by density irregularities (Hinkel-Lipsker et al. 1992;

Bale et al. 1998; Yin et al. 1999; Willes and Cairns 2001). In addition, localized Langmuir wavepackets will be compared with the predictions of strong turbulence "wave collapse" (Robinson 1997). Continuous provision of TDS and LFR amplitude statistics on the timescale of a few minutes, another unique aspect of S/WAVES will allow a connection between amplitude distributions on timescales of a wave packet and the timescale of $\approx 1$ minute.

The TDS will also observe ion acoustic and other low-frequency waves in the solar wind, for instance in corotating interaction regions and shocks. The field distributions and high-resolution time series, especially coupled with "burst" IMPACT and PLASTIC data, will constrain theories for the generation of these waves. New theoretical constraints will result from the time series of high temporal resolution electric field measurements provided by TDS and data from IMPACT and PLASTIC in their burst modes.

An additional goal of the S/WAVES TDS is the study of harmonic generation in Langmuir waves. Electromagnetic radiation at twice the plasma frequency is usually observed with the fundamental radiation near the plasma frequency, and even higher (but weaker) harmonics are observed (Cairns 1986). If Langmuir waves are converted to electromagnetic radiation on density ramps, then the mechanism for generation of the harmonic becomes a problem. Reflection on density ramps provides a convenient source of oppositely directed Langmuir waves to generate the harmonic by the traditional process of nonlinear interaction of such pairs of waves. It is, however, important to consider the harmonic content of the primary Langmuir waves, especially as electron trapping occurs only in the positive potential peaks of the waves and will lead to a second harmonic component. Whereas the earlier Wind-Waves TDS experiment had a non-linear A/D converter which made the study of harmonic generation difficult, the A/D converter used in the S/WAVES TDS is accurately linear, and will allow a definitive study of harmonics.

The TDS system also supplies signals to a part of S/WAVES, the Langmuir Waves Statistics (LWS) subsystem, which periodically provides a distribution of wave amplitudes. An earlier experiment on WIND, the WAVES instrument (Bougeret et al. 1995), provided much useful information on large amplitude Langmuir waves. As discussed in the science section, because small amplitudes are more common and may represent appreciable energy, we also need the distribution of Langmuir wave amplitudes to compare various theories with observations. Theories of conversion to electromagnetic modes and the Stochastic Growth Theory require this comparison. The Langmuir Wave Statistics (LWS) subsystem will provide a histogram of the distribution of wave amplitudes based on the largest signal detected by the TDS in a (commandable) period of about 20 msec. This histogram will be collected and telemetered about once per minute. Separate wave amplitude histograms are made simultaneously for each of the four TDS channels.

### 2.4.3 Low Rate Science (LRS)

This part of the instrument is designed to investigate:

(1) conversion of Langmuir waves into the electromagnetic signals of type II and type III solar radio bursts; and
(2) turbulent processes which are an important part of the behavior of the solar wind, particularly how it is heated and altered at 1 AU.

To carry out these objectives, the LRS will measure density fluctuations and electric fields, especially in the frequency range which would resonate with ions. Comparison of the observed density fluctuations with observations of Langmuir waves by the Time Domain Sampler (TDS) and radio parts of the experiment will determine whether conversion of Langmuir waves on density ramps is important in the production of radio bursts.

The three DC-coupled APM channels provide rapid measurements of plasma density, using a method similar to that described by Pedersen (1995), but modified because the antennas are not biased to float at the plasma potential. This method is based on the fact that the floating potential of a conducting body in a plasma depends on a competition between photoelectron emission, which is essentially constant, and ambient electron pickup, which depends on electron density and temperature. The floating potential also depends on the geometry of the photo-emitting and electron pickup surfaces, and is expected to be different, and to depend differently on density and temperature, for the antennas and spacecraft. There is no adequate theoretical basis to calculate *a priori* the relation between density and potential difference so this density measurement will be calibrated using density measurements by PLASTIC and IMPACT. When possible, measurements of the quasi-thermal plasma line will be used, in preference to the density measurement of the plasma instruments. Because the antennas are so short, the quasi-thermal plasma line is expected to be observable only during times when the halo part of the electron distribution is relatively large (i.e. at times of low total density). When it can be observed, however, it provides a more accurate measure of electron density as described below. The electric field measurements will be calibrated using the lower frequency $\mathbf{V_{sw}} \times \mathbf{B}$ field from PLASTIC and IMPACT.

## 2.5 Solar Wind Physics: Electric Field and Density Fluctuations

At periods longer than a few seconds, three dimensional electric fields in the solar wind have not been measured. As a result, little is known except for the expectation and measurement of a convection field $\mathbf{E} = -\mathbf{v} \times \mathbf{B}$. Kellogg and Lin (1997) pointed out that solar wind electric fields in the frequency range which would resonate with the cyclotron frequency of the ions had never been measured, and that such fields could act as collisions and have a determining effect on the particle distributions of the solar wind. This range, which is Doppler shifted to about one hertz, is very difficult to measure on a spinning satellite because photoelectric voltages are much larger and in the same frequency range.

Several efforts have been made to measure electric fields in this frequency range in the solar wind. Our first attempt was with the URAP experiment on Ulysses (Stone et al. 1992). The Ulysses spin axis is always pointed at the Earth, which reduces photoelectric variations when the axis is also pointed near the sun. However, leakage from the photoelectric variations was too large in the 1 Hz range, though frequencies above 10 Hz were measurable because a hardware filter eliminated the spin frequency (Lin et al. 2003). The next attempt was with the experiment RPWS on Cassini (Kellogg et al. 2001, 2003). Cassini is 3-axis stabilized, but an instability on the wake caused interference which prevented good measurements.

More recently, a successful attempt using the EFW experiment on the Cluster satellites has been made (Bale et al. 2005; Kellogg et al. 2006). Kellogg et al. (2006) showed that the electric fields are indeed strong, and that their effect on the ions is larger than the effect of magnetic field fluctuations. The Cluster spacecraft spin but use electric field probes which are designed to minimize photoelectron variations. As discussed more fully in Bale et al. (2005) and Kellogg et al. (2006), it is unclear whether the measurements at the high frequency end of the plateau are reliable. It is one of the objectives of the Low Rate Science system to settle this question. Cluster is not in the solar wind very much of the time, and is in the free solar wind (i.e. not connected to the Earth's bow shock or magnetosphere) even less often. Hence, having shown that electric fields in the ion cyclotron range are important, we will use the 3-axis stabilized STEREO spacecraft for studies of the occurrence and amplitude, correlation with other phenomena, etc. of these low frequency electric fields.

The measurement of rapid density fluctuations is an essential part of our efforts to understand the mechanism of generation of type II and type III radio bursts. In addition to being a part of solar wind turbulence which has been neglected in favor of studies of magnetic field and velocity turbulence, it has been suggested (Field 1956; Kellogg 1986; Bale et al. 1998; Willes and Cairns 2001) that density changes play an essential role in the conversion of Langmuir waves to electromagnetic radiation. It has been argued that density fluctuations account for the long, exponentially decaying tail of fundamental emission in type III solar radio bursts, via multiple scattering of the emitted radiation, and the non-integer fundamental to harmonic frequency ratio via mode conversion back to Langmuir waves (Kellogg 1986; Robinson and Cairns 1998a).

Sufficiently accurate and rapid measurements of density have been difficult to do with plasma instruments. Typical density fluctuations amount to one or a very few percent— of the same order as typical plasma instrument counting statistics when samples are made rapidly. Early measurements on Ogo 5 (Unti et al. 1973) and on ISEE (Celnikier et al. 1983, 1987) have determined these amplitudes using other techniques, as well as a spectrum which is close to, but not exactly, a descending power law.

## 3 Required Measurements

Figure 4 shows the overall instrument sensitivity that is required to fulfill the S/WAVES scientific objectives. Superimposed is the sensitivity actually obtained with S/WAVES. The shot noise on this curve corresponds to the noise induced by solar wind electrons and protons impacting on the antennas.
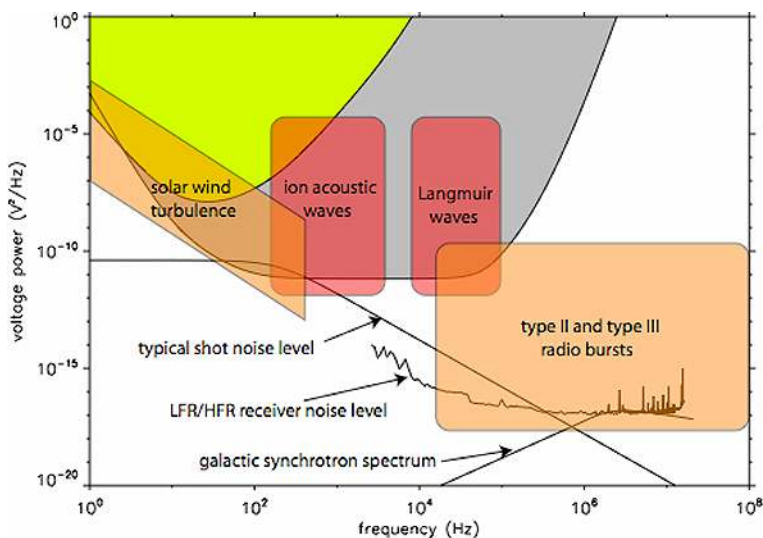


**Fig. 4** (Color online) Required and known sensitivity as a function of frequency. Typical levels of solar wind electric field turbulence, ion acoustic, and Langmuir wave power are shown, as well as IP radio burst levels. The galactic nonthermal continuum level and the expected shot noise levels will determine the actual measurement background. The *green area* shows the expected sensitivity of the LRS burst measurement, while the *grey area* shows the expected TDS sensitivity. Measured LFR and HFR noise levels are also shown

**Table 1** S/WAVES frequency domain parameters

|  | LFR | HFR | FFR |
|---|---|---|---|
| Frequency coverage | 2.5–160 kHz | 125–16.025 MHz | 30.025 or 32.025 MHz |
| Bandwidth | 2-octave | 25 kHz | 25 kHz |
| Frequency resolution | $\Delta F/Fo = 8.66\%$ | $\geq 50$ kHz | N/A |
| Sensitivity | 6 nV/Hz$^{1/2}$ | 6 nV/Hz$^{1/2}$ | 40 nV/Hz$^{1/2}$ |
| Dynamic range | 120 dB | 80 dB | 50 dB |

### 3.1 Frequency Domain Measurements

In order to carry out this scientific program, the remote-sensing part of S/WAVES consists of:

– the Fixed Frequency Reciever (FFR) for connection with ground based measurements
– the High Frequency Receivers (HFR) for spectral analysis and direction finding of radio noise generated from a few solar radii (16 MHz) to about half an Astronomical Unit (125 kHz)
– the Low Frequency Receiver (LFR) for spectral analysis and direction finding from about half an Astronomical Unit (160 kHz) to one AU (2.5 kHz).

Table 1 lists the measurement requirements for these receivers, described in more detail in the experiment description section.

### 3.2 Time Series Measurements

In order to carry out this scientific program, the in-situ part of S/WAVES consists of:

– The Time Domain Sampler (TDS) and its associated Langmuir Wave Statistics system (LWS) for measurement of the Langmuir waves which are the first stage of solar radio radiation. The TDS measurements will also measure density fluctuations on a time scale appropriate for their interaction with the Langmuir waves.
– The Low Rate Science (LRS) system for measurement of density fluctuations and of electric fields in the frequency range around the ion plasma frequency (0.03 to 32 Hz).
– The Antenna Potential Monitor (APM), for slow monitoring of plasma density changes.

These instruments will be described in more detail in the experiment description section.

### 3.3 Direction Finding capabilities of S/WAVES

Based on the Cassini/RPWS experiment (Gurnett et al. 2004), the S/WAVES radio receiver also has the capability for radio direction finding (also known as goniopolarimetry). From these measurements it is possible to ascertain the direction of arrival of an incoming electromagnetic wave (represented by two angles: the colatitude $\theta$ and azimuth $\phi$), its flux density ($S$), its polarization state (three Stokes parameters: $Q$ and $U$, the linear polarization degrees, and $V$ the circular polarization degree) and possibly the typical angular extension of the source ($\gamma$). The basic measurement obtained by S/WAVES is a set of four instantaneous measurements on a pair of electrical antennas: one autocorrelation on each of the two antennas and the complex cross-correlation between them.

For complete direction finding, there are seven unknowns ($\theta$, $\phi$, $S$, $Q$, $U$, $V$ and $\gamma$) but only 4 measurements (two autocorrelations and a complex cross correlation) in a single measurement cycle, so a single S/WAVES measurement does not contain enough independent

information with which to solve the system without assumptions on the wave parameters. To overcome this difficulty, two specialized direction finding modes allow making two or three basic measurements quasi-instantaneously. This is done by switching the antenna configuration at the receiver input as often as every measurement. With two successive measurements on two different pairs of antennas, we obtain seven independent measurements (three autocorrelations and two complex cross-correlations). For three successive measurements on three different pairs of antennas, there are nine independent measurements (three autocorrelations and three complex cross-correlations). The measurements must be inverted to solve for the source parameters.

The details of these inversions are discussed in Cecconi et al. (2007) which contains a more complete presentation of the direction finding capabilities of the S/WAVES experiment, as well as an insight into the kind of results that will be obtained based on the example of Cassini/RPWS observations of solar radio bursts.

### 3.4 Triangulation and Stereoscopic Measurements

To achieve the science goals discussed above, the S/WAVES investigation will make use of the full 2D radio direction finding measurements from the separate STEREO spacecraft. Combining S/WAVES observations from the two spacecraft will lead to three dimensional source location of radio emissions (triangulation) and stereoscopic measurements of their properties.

#### 3.4.1 Radio Triangulation

Radio triangulation can be performed at each sampled frequency by two different means, using 2D direction finding and the time of arrival of the radiation on each spacecraft.

(1) Triangulation with the directions of arrival of the radiation observed on the two spacecraft.
(2) Triangulation with the direction $D$ of arrival of the radiation on one spacecraft together with the difference $\Delta t$ of the arrival times measured at both spacecraft. This method assumes radio propagation in free space at the speed of light and the 3D location of the radio emission source will then be given by the intersection between $D$ and the hyperboloid of revolution where $\Delta t$ is constant.

Performed on a large statistical basis as a function of direction and using a combination of the two methods, comparison of these 3D source locations will provide insights into propagation effects at work, as shown previously in stereoscopic case studies by Steinberg et al. (1984) on the ISEE-3 and Voyager spacecraft and by Hoang et al. (1998) and Reiner et al. (1998c) on Ulysses and WIND.

In this way, the reliability of the determination of the radio source positions can be checked and the accuracy estimated. This is a crucial element in tracking interplanetary CME driven shocks that emit type II radio bursts. Another important advantage of direct radio triangulation is avoiding the use of a heliospheric density models (e.g., Saito et al. 1977; Leblanc et al. 1998) or simple $1/r^2$ density variation to convert the frequency scale to a distance scale.

#### 3.4.2 Stereoscopic Measurements of Radio Emission Properties

Stereoscopic direction finding measurements from both spacecraft with increasing viewing angles, made on large data sets, will allow derivation of statistical characteristics of the radio emission as a function of observing direction. The emission directivity, or beam pattern,

together with the source size and frequency drift rate, yields information on the emission mechanism, the radiation mode and on the propagation medium. From Ulysses-ARTEMIS observations of solar kilometric type III bursts, Poquerusse et al. (1996) and Hoang et al. (1997) reported the average radiation pattern of interplanetary type III bursts to be shifted significantly East of the radial direction. S/WAVES can study this important effect, as well as the directivity of the type II emission associated with interplanetary CME shocks.

### 3.5 Thermal Noise Spectroscopy in Solar Filamentary Material

Many CMEs originate in coronal prominences that are ejected violently from the sun by a mechanism that is not yet fully understood and which may include magnetic reconnection in some cases. These CMEs propagate in the interplanetary medium, carrying the magnetic field pattern from their parent prominence. The physical properties of these magnetic field structures, known as magnetic clouds, are not well known because of a lack of adequate observations. However we know they are fundamentally different from the ambient solar wind.

In magnetic clouds, electron distributions can be very dense and extremely cold (Larson et al. 2000). Traditional electrostatic analyzers have difficulty measuring electrons in this regime, as the illuminated spacecraft floats at several volts positive, making measurements at a few eV quite difficult.

Since particles and electrostatic waves are so closely coupled in a plasma, particle properties can often be determined by measuring waves. In a stable plasma, the particle thermal motions produce electrostatic fluctuations which are completely determined by the velocity distributions (and the static magnetic field). Hence, measurement of this quasi-thermal noise provides information on the density, temperature and relative numbers of core and halo electrons.

The technique of quasi-thermal noise spectroscopy (Meyer-Vernet and Perche 1989) can be used in the regime where the Debye length is small compared with the electric antenna length. This technique, which is based on the analysis of the wave spectrum measured by electric antennas, is not affected by the spacecraft potential. It is thus more accurate in this regime than traditional analyzers and can be used for absolute calibration.

In the solar wind, the electron gyrofrequency $f_{ce}$ is much smaller than the plasma frequency $f_p$. In this case, the electron thermal motions excite Langmuir waves, so that the quasi-equilibrium spectrum is cut-off at $f_p$, with a peak just above it (see Fig. 5). In addition, electrons passing within a Debye length, $L_D$, of the antenna induce voltage pulses on it,

**Fig. 5** Spectrogram measured by the WIND spacecraft on April 08, 2003. This spectrogram represents, as a function of time, the radio power spectral density in the frequency range between 16 to 256 kHz. One can clearly see the plasma peak varying on that day between roughly 25 and 90 kHz. This corresponds to density variations between roughly 8 and 100 cm$^{-3}$
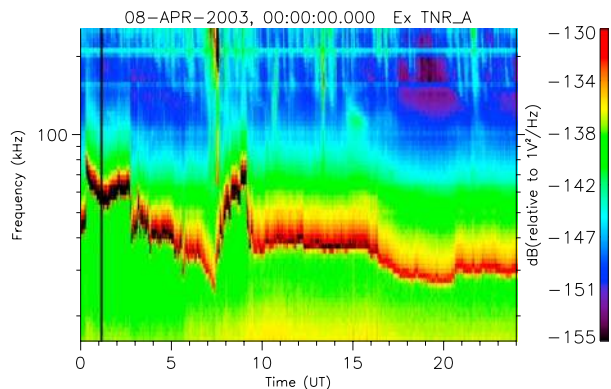
**Fig. 6** Typical spectrum measured on Ulysses. The *solid line* is the theoretical Quasi-thermal noise spectrum which best fits the data (*points*) within 1.6% of the standard deviation
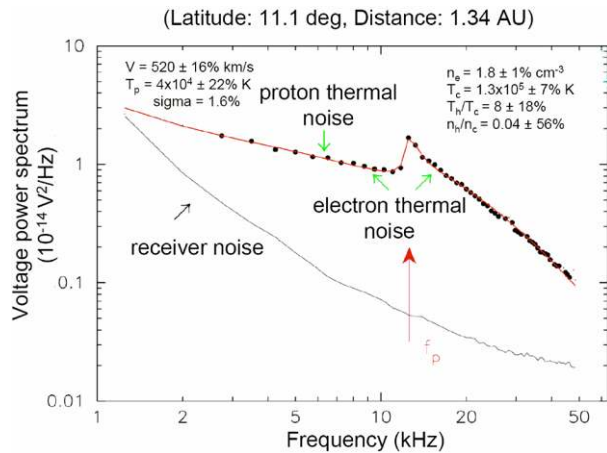


producing a plateau in the wave spectrum below $f_p$ and a decreasing level above $f_p$. Since $L_D$ is mainly determined by the bulk (core) electrons, the spectrum above $f_p$ gives information about the core population. In contrast, since the Langmuir wave phase velocity becomes infinite at $f_p$, the fine shape of the $f_p$ peak is determined by the fast (halo) electrons. Hence the quasi-thermal spectrum gives information on the whole electron distribution as well as giving an accurate measure of the total electron density.

When $f_{ce} \ll f_p$, measuring the thermal noise spectrum allows a precise determination of the electron density and bulk temperature (using respectively the cut-off at $f_p$ and the spectrum level and shape around it), whereas the detailed shape of the peak itself reveals the suprathermal electrons (Meyer-Vernet and Perche 1989; Meyer-Vernet et al. 1998). This method has yielded routine measurements of the solar wind electron plasma parameters for space missions such as Ulysses (Maksimovic et al. 1995; Hoang et al. 1996; Issautier et al. 1998) and WIND (Maksimovic et al. 1998). It has also been used in both magnetized and unmagnetized environments, for example, planetary magnetospheres (Moncuquet et al. 1995) and a cometary plasma tail (Meyer-Vernet et al. 1986).

Figures 5 and 6 show examples of quasi-thermal noise (QTN) observations in the solar wind. Figure 5 is a spectrogram measured by the WIND spacecraft on 8 April, 2003, plotting the power spectral density in the frequency range between 16 to 256 kHz as a function of time. One can clearly see the plasma peak varying on that day between roughly 25 and 90 kHz. This corresponds to density variations between roughly 8 and 100 cm$^{-3}$. Figure 6, adapted from Issautier et al. (2001a), shows a typical plasma spectrum on Ulysses, obtained in the solar wind, with an intense peak just above the local plasma frequency $f_p$. The spectral analysis yields the electron density and thermal temperature with a good accuracy, in addition to the solar wind speed (due to the Doppler-shifted thermal fluctuations of the ions), and suprathermal parameters (Issautier et al. 1999). Note that the density measurement is independent of any calibration gain determination, since it relies directly on a frequency determination that is usually very accurate.

QTN spectroscopy is almost immune to the limitations due to spacecraft charging due to the fact that, close to the local plasma frequency, the antenna is sensitive to Langmuir waves with very large wavelengths. At the plasma frequency peak the antenna samples an average over a large plasma volume. Therefore TN spectroscopy has been used to calibrate the density and temperature obtained by the electron analyzers, which are usually perturbed by spacecraft charging effects.

Maksimovic et al. (1995) and Issautier et al. (2001b) performed detailed comparisons between the two kind of instruments on Ulysses and emphasized that the TN spectroscopy method is a complementary tool to cross-check other techniques for determining electron densities. Moreover, it is important to note that, using QTN electron densities, it is possible to improve the determination of the spacecraft potential, and thus to correct the electron parameters determined by particle spectrometers (Maksimovic et al. 1998; Salem et al. 2001).

## 4 Instrument Description

### 4.1 Introduction

The S/WAVES instrument is shown schematically in Fig. 7. There are a number of related subsystems which are described in detail in the following sections. On the left are the antennas and their deployment units. Within the antenna assembly is a preamplifier enclosure which houses all of the preamplifiers. The amplified signals from the preamplifier connect to a number of receivers. The Low Frequency Receiver (LFR), a spectrum analysis receiver, and the High Frequency Receiver (HFR), a super-heterodyne swept frequency receiver connect to a dedicated Digital Signal Processor unit. A Fixed Frequency Receiver (FFR) at about 32 MHz provides in-flight measurements which can be compared to ground observations. The signals also feed the time series receivers: the Time Domain Sampler (TDS) which includes the Langmuir Waves Statistics histogram, and the Low Rate Science (LRS) subsystem. All of the data then flows into the Data Processing Unit (DPU) and then to the spacecraft data handling system.

### 4.2 Antennas/Sensors

S/WAVES measures the fluctuation electric field present on three orthogonal monopole antennas mounted on the back (anti-sunward) surface of the spacecraft. Each monopole antenna unit is a 6 m long Beryllium-Copper (BeCu) "stacer" spring. The three units deploy from a common baseplate that also accommodates the preamplifier housing (see Fig. 8). The 6 m length was chosen to put the antenna quarter-wave resonance near the top of the S/WAVES HFR2 frequency band. The details of the antenna design are reported in a separate paper (Bale et al. 2007).
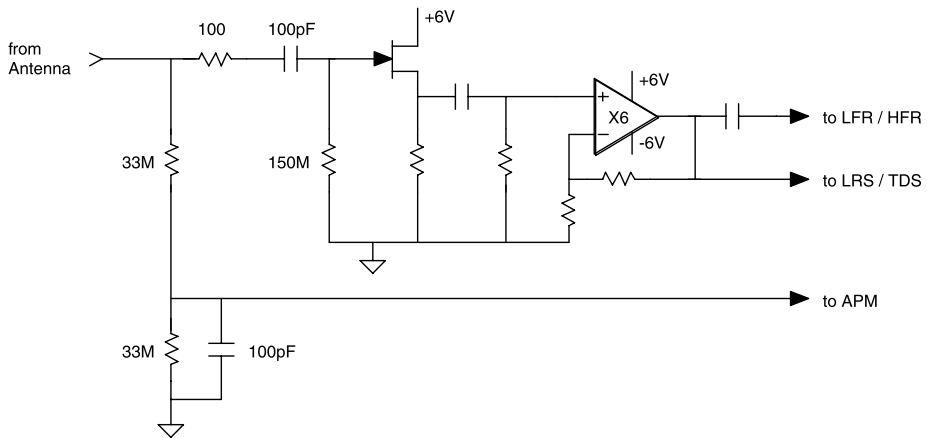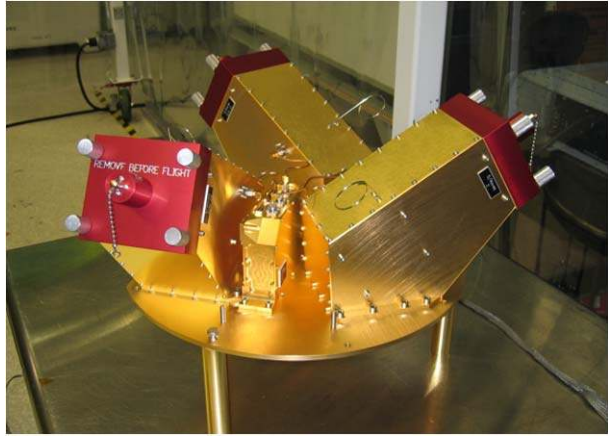
### 4.3 Preamplifiers

The three electric monopoles are connected to low noise and high impedance preamplifiers located close to the base of the deployment mechanism. This is required to minimize the effect of the base capacity, which can severely limit the sensitivity of the receiver. As shown in Fig. 9, below, each preamplifier channel has a single FET (field effect transistor) at its input and provides three outputs: one with AC coupling for the frequency domain analyzers (LFR and HFR), another with AC coupling for the time domain analyzer (TDS) and one with DC coupling for antenna and spacecraft potential monitoring. This path also provides a path from the antenna elements to the spacecraft ground (through a large resistance) to avoid having the elements become highly charged. Three additional preamplifiers are specifically dedicated to the Fixed Frequency Receiver (FFR). The FFR preamplifiers are connected to the three monopoles, allowing the FFR to be connected to one of three pseudo-dipole combinations $Ex/Ey$, $Ey/Ez$ or $Ex/Ez$.
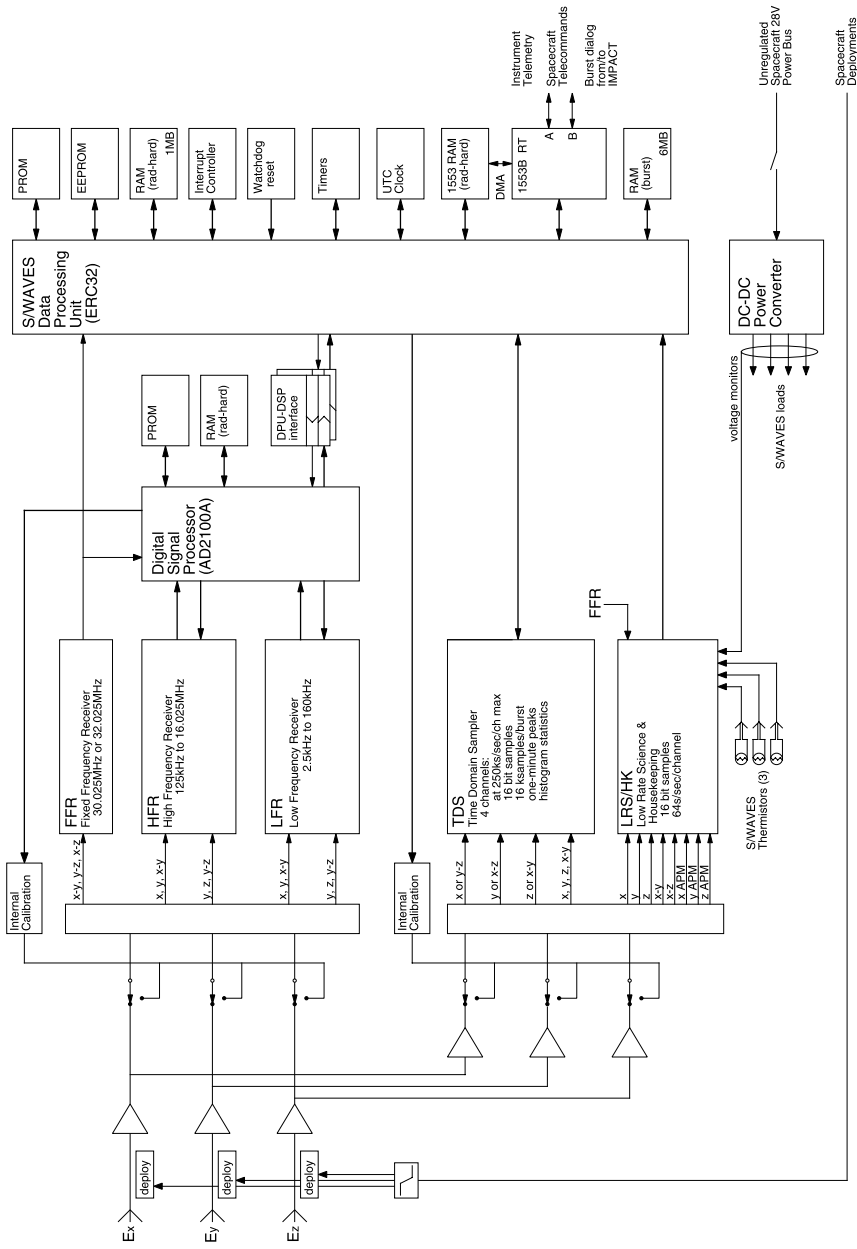
**Fig. 7** The overall block diagram of the S/WAVES instrument

**Fig. 8** The S/WAVES antenna assembly with three mutually orthogonal antenna elements (stowed and protected with retaining covers) and preamplifier enclosure





**Fig. 9** A typical preamplifier circuit

## 4.4 The Low Frequency Receivers (LFR)

The LFR is a direct conversion receiver for spectral processing from 2.5 kHz up to 160 kHz. This frequency range is divided into three 2-octave bands with sharp anti-aliasing analog filters. Except for band A (2.5–10 kHz), the LFR front end has two channels which are essential for the processing of the cross correlation used in direction finding. In normal operation, each 2-octave band is sequentially connected to the antennas and simultaneously sampled on both channels. The LFR block diagram is shown in Fig. 10.

Using a wavelet-like transform, the digital spectral analysis is processed in each 2-octave band with 16 logarithmically-spaced frequencies, leading to a 8.66% spectral resolution. This results in a total of 48 log-spaced frequencies (Table 2).

The LFR is intended to cover a broad dynamic range with a constant amplitude resolution over the whole range. This implies that the receiver is able to adjust its gain according to the input level. An Automatic Gain Control (AGC) determines the receiver gain on a logarithmic scale as a function of the input level. The LFR analog front end normalizes the signal amplitude with an allowable gain variation of 80 dB. Combined with 12-bit analog to
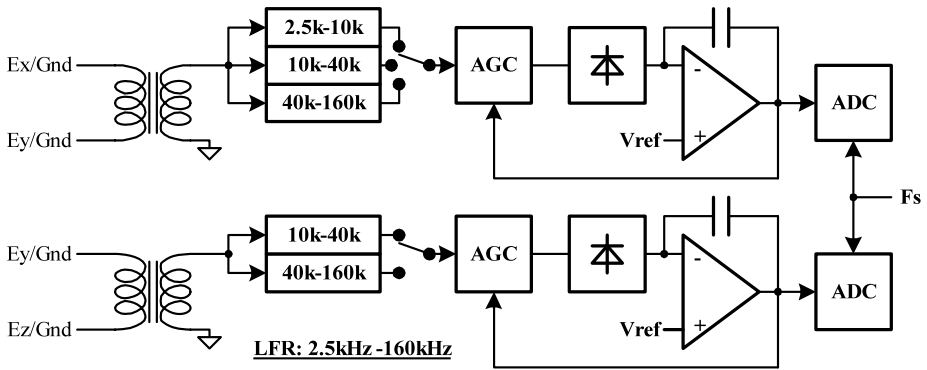
**Fig. 10** LFR block diagram

**Table 2** LFR frequency coverage

| Band | Frequency coverage (kHz) | Channels | Frequencies |
|------|--------------------------|----------|-------------|
| A | 2.5–10 | 1 channel | 16 log-spaced |
| B | 10–40 | 2 channels | 16 log-spaced |
| C | 40–160 | 2 channels | 16 log-spaced |

**Table 3** LFR/HFR antenna combinations

| Band | Channel 1 | Channel 2 |
|------|-----------|-----------|
| A | Off | X |
| | $Ex$ | X |
| | $Ey$ | X |
| | $Ey/Ex$ | X |
| B, C & HF | Off | Off |
| | $Ex$ | $Ey$ |
| | $Ex$ | $Ez$ |
| | $Ey$ | $Ez$ |
| | $Ex$ | $Ey/Ez$ |
| | $Ey/Ex$ | $Ez$ |

digital converters, the LFR provides a total dynamic range of 120 dB. The LFR sensitivity is 6 nV/Hz$^{1/2}$ at the preamplifier input. These characteristics are indispensable to accurate plasma wave measurements over a large dynamic range.

Various antenna configurations are available by command. The LFR can be switched to use either to pseudo-dipoles ($Ey/Ex$ or $Ey/Ez$) or monopoles ($Ex$, $Ey$ or $Ez$). Table 3 gives the possible antennas combinations.

The two channel receiver allows the production of auto-correlations as well as complex cross-correlations. These measurements can be made between any of the antenna combinations mentioned above. This is especially important for direction finding processing which can be performed in two different modes. The first mode consists of a two step analysis,

**Fig. 11** HFR block diagram
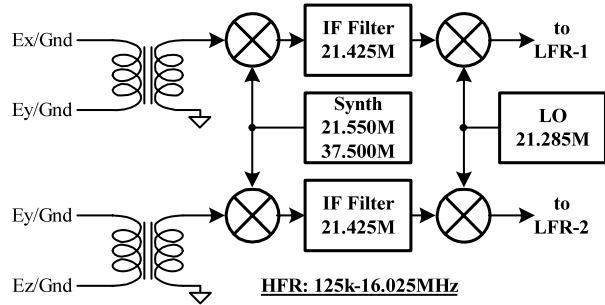


combining dipoles and monopoles ($Ex/Ey-Ez$ and $Ex-Ez/Ey$). The second mode is a three-step sequence combining the three monopoles ($Ex-Ey$, $Ey-Ez$ and $Ex-Ez$).

### 4.5 The High Frequency Receivers (HFR)

The HFR is a dual sweeping receiver operating in the frequency range 125 kHz–16.025 MHz. Using a super-heterodyne technique, the signal from the selected antenna is down-converted using mixers and a programmable synthesizer. The synthesizer produces frequencies at odd multiples of 25 kHz. This intermediate frequency signal is then sharply filtered such that a comb filter across the HF band is the result. The rejection of noise at even multiples of 25 kHz is 62 dB. This filtering scheme allows S/WAVES to sample between lines of noise that may be produced by power supply harmonics at multiples of 50 kHz (even multiples of 25 kHz). The odd/even "picket fence" technique allows for the coexistence of a very sensitive radio receiver and sometimes noisy spacecraft power supplies. Frequency shifted down, the finished signal is handled by the same LFR digitization and analysis hardware (described above) at a comparatively low digitization sample rate. The HFR provides a total dynamic range of 80 dB and its sensitivity at the preamplifier input is 6 nV/Hz$^{1/2}$. The HFR block diagram is shown in Fig. 11.

The receiving frequency is determined by a programmable synthesizer which covers the HFR spectrum from 125 kHz to 16.025 MHz with 50 kHz increments. Thus, the highest spectral resolution is 50 kHz and can be configured to multiples of 50 kHz by command. The time resolution is also adjustable depending on the integration time.

In a manner similar to the LFR, the antennas are configurable as monopoles or dipoles (see Table 3). The direction finding is performed using the same modes as the LFR.

#### 4.5.1 Digital Signal Processing Unit

To support the in-flight signal processing and data stream, the LFR and HFR front ends are connected to a digital signal processing unit. The conditioned analog signals are simultaneously digitized with 12-bit resolution on both channels. The time series sampling rate is selected to be appropriate to the selected band as listed in Table 5.

Digital filtering and the correlation calculation are the core of the signal processing. The digital filters are of the Finite Impulse Response (FIR) type and their coefficients have been determined by an optimization program. Their maximum length is 341 taps for the LFR and 191 taps for the HFR. This results in a bandwidth of 8.66% of the corresponding LFR frequency, and 12.5 kHz for the whole HFR frequency range. The digital filtering gives an out-of-band rejection greater than 70 dB, determined by the 12-bit digitization. Table 4 gives the digital filtering characteristics.

**Table 4** Digital filtering characteristics

| Band A | | Band B | | Band C | | Band HF | |
| --- | --- | --- | --- | --- | --- | --- | --- |
| $F_s = 40.625$ kHz | | $F_s = 162.500$ kHz | | $F_s = 464.286$ kHz | | $F_s = 464.286$ kHz | |
| $\Delta F_{(-3\ \mathrm{dB})}/F_o = 8.66\%$ | | $\Delta F_{(-3\ \mathrm{dB})}/F_o = 8.66\%$ | | $\Delta F_{(-3\ \mathrm{dB})}/F_o = 8.66\%$ | | $\Delta F_{(-3\ \mathrm{dB})} = 12.5$ kHz | |
| $F_o$ (kHz) | # taps | $F_o$ (kHz) | # taps | $F_o$ (kHz) | # taps | $F_o$ (kHz) | # taps |
| 2.61 | 341 | 10.45 | 341 | 41.81 | 245 | 140 | 191 |
| 2.85 | 313 | 11.40 | 313 | 45.59 | 225 | | |
| 3.11 | 287 | 12.43 | 287 | 49.72 | 207 | | |
| 3.39 | 263 | 13.56 | 263 | 54.22 | 189 | | |
| 3.70 | 241 | 14.78 | 241 | 59.13 | 173 | | |
| 4.03 | 221 | 16.12 | 221 | 64.48 | 159 | | |
| 4.40 | 203 | 17.58 | 203 | 70.32 | 145 | | |
| 4.79 | 185 | 19.17 | 185 | 76.68 | 133 | | |
| 5.23 | 169 | 20.91 | 169 | 83.62 | 121 | | |
| 5.70 | 155 | 22.78 | 155 | 91.19 | 111 | | |
| 6.22 | 143 | 24.86 | 143 | 99.44 | 103 | | |
| 6.78 | 131 | 27.11 | 131 | 108.44 | 93 | | |
| 7.39 | 119 | 29.56 | 119 | 118.26 | 85 | | |
| 8.06 | 109 | 32.24 | 109 | 128.96 | 79 | | |
| 8.79 | 101 | 35.16 | 101 | 140.63 | 71 | | |
| 9.59 | 91 | 38.34 | 91 | 153.36 | 65 | | |

Auto-correlations and complex cross-correlations are calculated for the 16 frequencies of each LFR band. The resulting calculations are compressed into 12-bit words and sent to the DPU in a compressed floating point format through a parallel interface. The auto-correlations are coded using a 5-bit exponent and a 7-bit mantissa while the cross-correlation requires a sign-bit with a 5-bit exponent and a 6-bit mantissa.

The measurement cycles are defined by the integration time which is set to produce acceptable statistical variations. The time needed for a block acquisition is inversely proportional to the frequency band of interest. This directly affects the temporal resolution which increases almost linearly with the integration time, as shown in Table 5.

## 4.6 The Fixed Frequency Receiver (FFR)

The S/WAVES package includes a fixed frequency receiver which consists of a single channel super-heterodyne receiver operating around 31 MHz. Depending on the response after launch, the frequency will be switched to either of two frequencies, 30.025 MHz or 32.025 MHz.

The FFR detects the incoming signal to produce a slowly varying voltage which is logarithmically proportional to the input level. Its sensitivity is about 40 nV/Hz$^{1/2}$ with a dynamic range of about 50 dB. The FFR block diagram is shown in Fig. 12.

The DC voltage is sampled directly by the DPU at 64 samples per second. To reduce noise the resulting time series is filtered with a variable length median filter to a few samples per second before transmission to the ground.

**Table 5** DSP integration time parameters

| Band | Sampling rate (kHz) | Effective period (ms) | Number of blocks | Integration time (ms) | Time res. (ms) |
|------|------|------|------|------|------|
| A | | | 42 | 125/**1** | 406 ± 1 |
| 2.5–10 kHz | 40.625 | 2.988 | 84 | 250/**1** | 800 ± 1 |
| | | | 168 | 500/**1** | 1590 ± 1 |
| | | | 336 | 1000/**1** | 3180 ± 1 |
| B | | | 42 | 125/**4** | 182 ± 1 |
| 10–40 kHz | 162.500 | 0.747 | 84 | 250/**4** | 356 ± 1 |
| | | | 168 | 500/**4** | 704 ± 1 |
| | | | 336 | 1000/**4** | 1420 ± 1 |
| C | | | 42 | 125/**16** | 96 ± 1 |
| 40–160 kHz | 464.286 | 0.188 | 84 | 250/**16** | 184 ± 1 |
| | | | 168 | 500/**16** | 364 ± 1 |
| | | | 336 | 1000/**16** | 748 ± 1 |
| HF | | | 29 | 2.5 | 36 ± 1 |
| 125–16 MHz | 464.286 | 0.085 | 58 | 5 | 63 ± 1 |
| | | | 116 | 10 | 117 ± 1 |
| | | | 232 | 20 | 224 ± 1 |
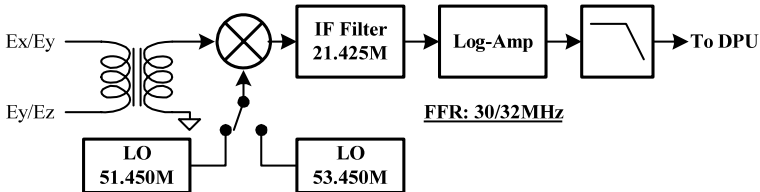


**Fig. 12** FFR block diagram

## 4.7 The Time Domain Sampler (TDS)

The Time Domain Sampler makes rapid samples of waveforms and is intended primarily for the study of Langmuir waves, waves at the plasma frequency and the precursors of type II and III radio bursts. Other wave modes, such as ion acoustic waves, can also be studied. The rapid simultaneous sampling of three orthogonal antennas as well as a pseudo-dipole channel obtained by taking the difference of any two monopoles allows the study of waveforms, their distortions, and, through ground-based Fourier analysis, a frequency determination which is far more accurate than any possible on-board filter analysis system.

Analysis of data from the TDS of WIND/WAVES (Bougeret et al. 1995) provided major contributions to our understanding of Langmuir waves in the solar wind. The TDS of S/WAVES is a similar, but improved instrument.

The TDS (Time Domain Sampler) provides for rapid sampling of transient events in the time domain. Its objective is to make very fast samples while also making effective use of the telemetry downlink. The maximum continuous sampling speed of the TDS is 16 million
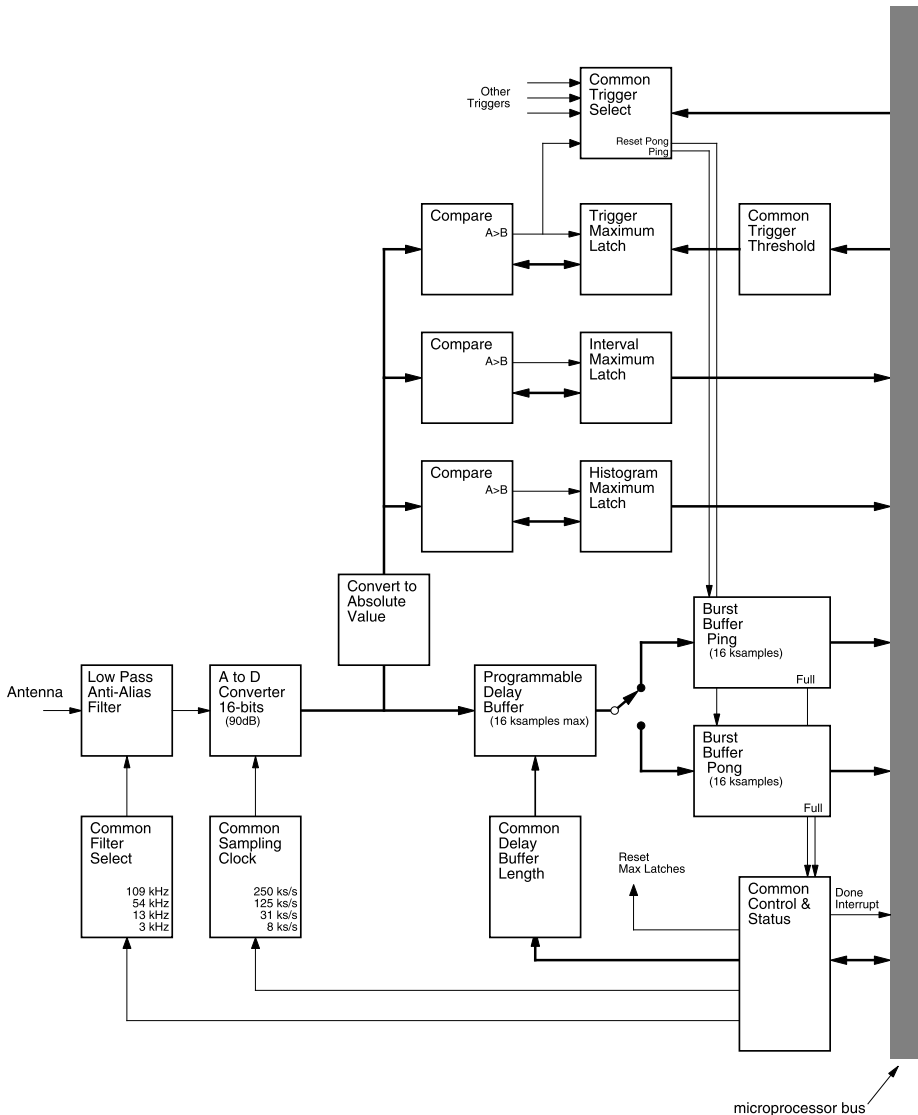
**Fig. 13** A block diagram of one (of four) TDS channel

bits per second. The typical TDS share of the S/WAVES downlink rate is only about 500 bits per second. The TDS achieves that large reduction in bit-rate while maintaining high scientific return by choosing events for transmission to the ground intelligently.

The TDS functions like a modern digital oscilloscope. It samples the voltage on the S/WAVES antennas quickly and continuously. When the sampled amplitude exceeds a commandable threshold (as described below), a triggering system takes a snapshot with the largest part of the signal at the center of the time series. A typical event from one channel is shown in Fig. 14.

**Fig. 14** A typical Langmuir wave packet from the TDS
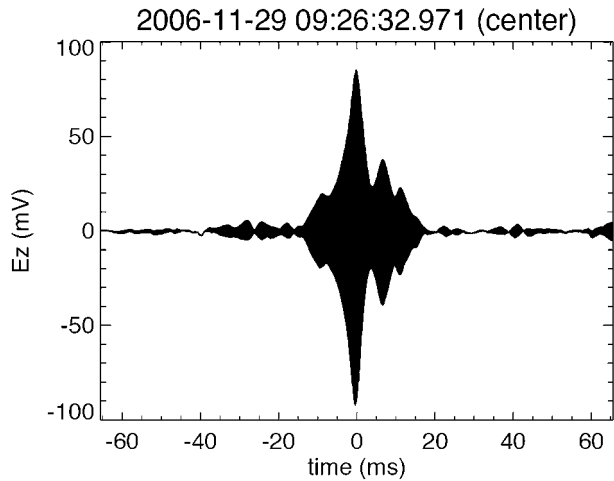


**Table 6** TDS characteristics

|   | Sample speed (s/s) | Low pass filter (kHz) | Maximum duration (ms) |
|---|---|---|---|
| A | 250,000 | 108 | 66 |
| B | 125,000 | 54 | 131 |
| C | 31,250 | 13.5 | 524 |
| D | 7,812.5 | 3.375 | 2,097 |

The TDS gathers events on four channels simultaneously. The commandable sampling times are listed in Table 6 with 250,000 samples per second the fastest sampling speed. This gives a Nyquist frequency of 125 kHz. Events can be as long as 16,384 samples, giving a maximum event duration of about 2 seconds. This gives a lower frequency bound of 0.5 Hz. The DPU's 6 MB burst memory provides storage for about 40 full events, each of which has 4 channels. Software criteria determine the effective quality of each event and, in general, the events with the highest quality are selected for transmission to the ground.

The TDS has four input channels connected to commandable combinations of the S/WAVES antenna system. Its nominal mode of operation is to have the three S/WAVES monopole antennas connected to each of three input channels while the fourth channel is connected to a pseudo-dipole obtained from the analog difference between two monopoles. The commandable switching network allows for full capability even with a failure of one channel.

Figure 13 is a block diagram of one of the four TDS acquisition channels. The selected analog signal is first filtered with a commandable bank of low pass filters to avoid aliasing. In general, the low pass filter (as shown in Table 6) is selected to match the current sampling speed. The effects of these simple filters are shown in Fig. 15 which gives the complete frequency response of the TDS including the four selectable low pass filters.

After filtering, the analog signals are digitized. Each of the four channels is digitized simultaneously by one of four analog to digital converters (ADC). The ADCs used here provide 16 bits of dynamic range and are quite linear over the range. The digitized signals are then made available to a number of parts of S/WAVES. While these commercial parts are acceptable in their tolerance of total radiation dose, it is possible they could latch-up in

**Fig. 15** The gain of the time domain parts of S/WAVES. *Discrete points* represent measurements. *Lines* represent theory. The negative APM gain (i.e. gain less than unity) is multiplied by 100 for visibility. Different TDS *curves* reflect selectable low pass filters
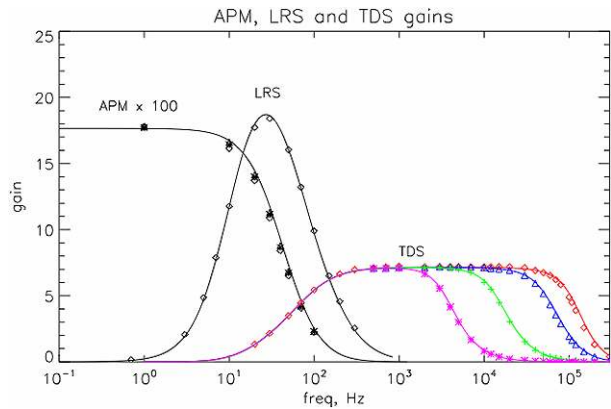
the presence of energetic particles. To prevent permanent damage, the ADCs are protected by a circuit breaker which shuts off power when high current is detected, allowing parasitic currents within the device to dissipate. The S/WAVES DPU normally turns the converters back on after a programmable cooling-off period (nominally 5 seconds).

For the TDS itself, the outputs of each of the four ADCs enter digital comparators. Each comparator examines the incoming stream of digital samples, searching for a new input value that is arithmetically larger than the value currently latched in its memory. Upon finding a larger value, the new value is latched for later comparisons and a trigger pulse is produced. One of the four trigger pulses is used to reset or clear the TDS hardware burst buffers. At initialization and after the collection of each full event, the comparator memories are initially set to a commandable threshold value. Setting the threshold to a value just above the noise level can be used to limit the number of "small" or uninteresting events acquired by the system. While each of the four channels has trigger generation logic, one is commanded as the trigger source for all TDS channels at any given time.

The digitized signals are also sent into a digital delay buffer. The delay buffer is simply a first-in-first-out memory which provides for a commandable delay time. The memory can provide delays of from one to 16,383 samples. Setting the delay time allows the peak value of an event to appear anywhere in the event. The delay buffer length is typically set to half the length of the event itself giving an event with a peak in its center.

After a programmable delay, the digital values emerge from the delay buffers and enter the burst buffers. Each burst buffer is another first-in-first-out memory in which 16,384 samples are obtained from the output of the digital delay buffer. As these buffers are being filled, they are reset by one of the digital comparators as larger signals are obtained. At the start of an event, the resets occur rapidly but as the comparator obtains increasingly large values, the resets stop. Shortly thereafter, the burst buffer becomes full, indicating that a complete event has been acquired on all four channels.

When a burst buffer is full, the DPU copies the completed event from the burst buffers to TDS burst memory. While the DPU is reading out the contents of the burst buffer, the burst buffer is unable to begin storing a new event. To prevent a reduction in the acquisition of possibly good events during the comparatively long copying period, there are dual or ping-pong burst buffers which alternate such that one burst buffer can be acquiring a new event while the previous event in the other buffer is being emptied by the DPU. After the event has been completely copied by the DPU, a new event can begin filling the burst buffer.

When a new event is acquired, the DPU time-stamps the new event and begins the process of copying it from the burst buffer to burst memory, which is a large part of the DPU memory

dedicated to storing about 40 4-channel TDS events for eventual transmission to the ground. Once the event has been copied, the DPU invokes a process to determine the "quality" of the new event. With changes in flight software, the quality determination could be any arithmetic evaluation of the event. In this way, the "best" events are sent to the ground.

When a new event is ready to be copied from the burst buffer to burst memory, the DPU discards the existing event with lowest quality to make room for the new event. An event's quality assignment is also used when space becomes available in the telemetry stream for a new TDS event. At that time, the DPU examines the pool of events in the burst memory and sends the event with the highest quality to the ground. This quality information can also be used (as described below in Sect. 5.3) to trigger simultaneous bursts with the IMPACT instrument and vice-versa.

In addition to sending events with high quality to the telemetry stream, the TDS also maintains a separate stream of events which are selected at random, without regard to their quality. The relative proportion of such "honest" events to "quality" events can be changed by command. This prevents having the TDS send "good" events to the exclusion of other, perhaps still interesting events with small quality values (e.g., smaller amplitude).

While the sensitivity of the TDS depends on frequency, in practice the noise level for each channel is less than 10 µV RMS (at about 10 kHz) at the input to the preamplifier. The largest signal obtained before saturation is about 125 mV RMS. To relate observations to actual observed electric field strength depends both on the frequency (as shown in Fig. 15) and the effective antenna length (see Bale et al. 2007).

## 4.8 Langmuir Waves Statistics (LWS)

As described above in Sect. 4.7, the TDS part of S/WAVES gathers data continuously at a high sampling rate. It examines the stream of data and sends "interesting" events to the ground. This often results in clusters of events where all the events of a cluster are acquired in a few minutes. These clusters, which based on WIND observations will usually be Langmuir waves (but could have other causes), are often separated by many hours.

The Langmuir Waves Statistics (LWS) subsystem is intended to fill in the gaps between clusters of TDS events. This subsystem uses the stream of digitized signals as described in Sect. 4.7 above. After low pass filtering, the TDS produces four continuous streams of digital data sampled at a commandable sampling rate defined in Table 6. In addition to flowing to the TDS, these streams flow to a set of digital comparators for the LWS subsystem as shown in Fig. 13.

Each comparator examines the incoming stream of digital samples. Each new value is compared to a value previously saved in the comparator. When the new value is arithmetically larger than the value currently latched in the comparator's memory, the new value is retained for future comparisons. Under software control, the S/WAVES DPU examines the saved contents of the comparator at a programmable interval. Each time the DPU examines the saved value, the saved value is reset (set to zero) such that a new search for a peak amplitude value begins.

In this way, the LWS comparators always contain the largest amplitude values observed during the preceding collection interval. Under software control, the DPU typically obtains the peak value from an LWS comparator once every 5,000 TDS samples. The number of samples for this interval can be changed by command and gives a time period of 20 ms at the highest TDS sampling speed. The LWS software uses the most significant 8 bits of the digital peak value as an address to one bin of a 256 bin histogram and increments the addressed location by one. The number of TDS channels used, the number of histogram bins

(i.e. the number of bits used) and the use of sign bits are characteristics that are determined by flight software and may be changed and optimized at some future time based on flight experience.

After a commandable number of collection intervals, the LWS software closes the finished histogram and formats it for telemetry. The number of collection intervals is 500 by default but can be commanded to give much longer collection periods and nearly 100% coverage of TDS samples. The resulting histogram(s) of peak amplitude distribution give a statistical view of peak wave amplitudes during the period regardless of the number or size of TDS events in the same period.

### 4.9 Low Rate Science (LRS)

The Low Rate Science (LRS) system is intended to make electric field and density measurements at a rate which encompasses the ion cyclotron frequency and other characteristic low frequencies of the plasma. It samples 8 channels at a rate of 64 samples per second. The characteristics of these channels are shown in Table 7. The gains of the various components are shown in Fig. 15. The discrete points are measured values of the gain, made by applying known sine waves to the preamplifier inputs. The solid lines are the theoretical magnitudes of the complex gains calculated from the circuit diagram. In Fig. 15, the negative gain (i.e. the gain is less than one) of the APM has been multiplied by 100 so that it will be readable.

After filtering, the analog signals from the antenna preamplifiers are digitized. Each of the eight LRS channels is digitized in series by a single analog to digital converter (ADC) with a network of multiplexers to switch amongst the analog inputs. In addition to the eight LRS channels, a number of other housekeeping values are multiplexed and sampled at the same cadence.

The sampling rate for the LRS channels is 64 samples per second. This rate was chosen to be exactly twice the sampling rate of the IMPACT magnetometer (see Acuña et al. 2007) to allow good correspondence between the two sets of data. Although there is only one ADC, an effort was made to sample the eight LRS channels at nearly the same time and with minimal jitter in the acquisition time. In order to prevent software-induced jitter in the acquisition times, a hardware acquisition system was developed to acquire the samples under hardware control. A hardware acquisition sequence is started 64 times per second. Within a sequence, each sample of the set of LRS values is acquired only 122 microseconds (=1/8192 seconds) after one sampled before it (as defined in Table 7).

The ADC used here provides 16 bits of dynamic range and is quite linear over the range. As with the TDS (described above), this commercial part could latch-up in the presence of

| Table 7  LRS characteristics | Channel number | Channel name | Frequency response |
|---|---|---|---|
| | 1 | $Ex$ APM | DC |
| | 2 | $Ey$ APM | DC |
| | 3 | $Ez$ APM | DC |
| | 4 | $Ex$ LRS | >0.03 Hz |
| | 5 | $Ey$ LRS | >0.03 Hz |
| | 6 | $Ez$ LRS | >0.03 Hz |
| | 7 | $Ex-Ey$ LRS | >0.03 Hz |
| | 8 | $Ex-Ez$ LRS | >0.03 Hz |

energetic particles and is protected by a circuit breaker which shuts off power when a high current is detected.

While the sensitivity of the LRS depends on frequency, in practice the noise level for the five AC-coupled LRS channels is less than 10 µV RMS (at about 10 Hz) at the input to the preamplifier. The largest signal obtained before saturation is about 70 mV RMS. The three DC-coupled APM channels have a range of $\pm 7$ V DC and are accurate to about $\pm 1$ mV. To relate observations to actual observed electric field intensity depends both on the frequency (shown in Fig. 15) and the effective antenna length (see Bale et al. 2007).

### 4.9.1 Low Rate Science Housekeeping

To give a broad and continuous picture of the DC antenna potentials and the other LRS quantities, they are included in the S/WAVES housekeeping telemetry. Once each minute, the DPU gathers the diverse information of the instrument housekeeping. This includes an instantaneous sample of the most recently acquired LRS values.

### 4.9.2 Low Rate Science Bursts

To allow more direct comparisons with both the TDS and particle measurements, the eight channels of LRS data are also saved in a ring buffer in the DPU memory. The buffer is filled at 64 samples per second, the normal acquisition rate of the LRS. The ring holds 8,192 continuous samples from each of the 8 LRS channels. When the instrument triggers, it causes an LRS burst snapshot be taken. A commandable number of samples is then formatted for telemetry from each of the eight LRS channels. The number of samples in a channel's burst is typically 2,048 (although events can be shorter or as long as 8,192) which corresponds to 32 seconds of LRS time series data.

The default triggering mechanism for these bursts is simply to take a snapshot whenever the telemetry stream has room for an LRS burst. It is also possible to generate a burst using a telecommand as the trigger or using information from the IMPACT instrument (see Sect. 5.3). It is planned that other triggering modes will be developed.

### 4.10 Data Processing Unit (DPU)

The heart of the S/WAVES instrument is its Data Processing Unit (DPU). The DPU is based on an ERC32 microprocessor developed by and for the European Space Agency at ESTEC. The RISC processor is an implementation of the SPARC V7 architecture. The commercial part is radiation hard and is produced by Atmel as the TSC695. The processor is a modern processor with 32 bit address and data busses.

As shown in Fig. 7, the DPU's processor is equipped with a 32 kB boot PROM, 512 kB of electrically erasable memory (EEPROM) and 1 MB of radiation-hard RAM. In addition to the rad-hard RAM, another 6 MB of radiation-tolerant RAM are dedicated to TDS and LRS bursts. This memory is larger but also slightly more susceptible to upsets but is used only for temporary data storage and not for instrument operation. A number of peripheral devices such as an interrupt controller, timers and counters are implemented in an FPGA connected to the processor.

The DPU communicates to the spacecraft using a MIL-STD 1553 communications bus. This interface is memory mapped into the processor's address space and uses direct memory access (DMA) as well as interrupts to communicate with the processor. The DPU receives telecommands and sends telemetry using this interface. The DPU also sends and receives

status messages and communicates with the IMPACT instrument with this interface. One of the status messages from the spacecraft provides the DPU with the current UTC time once each second.

The DPU also has a number of memory mapped devices which connect to the various S/WAVES science subsystems. A combination serial/parallel interface allows communication with the Digital Signal Processor (the HFR and LFR). The TDS and LRS subsystems are simply direct memory mapped interfaces.

With the application of power (or by command or watchdog time-out), the DPU's processor boots from reliable rad-hard PROM. Boot loader software burned into PROM before launch executes a simple boot loader program. The boot loader examines the contents of certain memory locations in RAM and in EEPROM in search of a valid block of executable flight software. In normal circumstances, a valid block is located in one of two banks of EEPROM memory. The boot loader copies the valid block of software into RAM and, after verifying the integrity of the block, transfer control to the flight software in RAM.

In normal circumstances, one copy of flight software is kept in the prime EEPROM bank and another version is kept in the backup location. This allows for reliable and safe operation even at times when the flight software in one EEPROM bank is being replaced by ground command. Once per hour during the mission, the EEPROM banks are checked for continued validity with the results reported in instrument housekeeping.

The S/WAVES DPU runs the RTEMS real-time operating system. RTEMS is a preemptive multi-tasking operating system which supports the various pieces of flight software. At the time of launch, the flight software had about 30 processes running and communicating using the RTEMS system.

## 4.11 Power Supply

The S/WAVES instrument includes a low voltage power supply. The STEREO spacecraft supplies S/WAVES with a single unregulated power service ranging from 22 to 36 volts. In order to produce a number of isolated but well regulated power services for the S/WAVES subsystems, the converter is built with a two stage design. The first stage uses a pulse width modulation technique to produce an intermediate voltage of 12 volts. This intermediate voltage is carefully controlled and provides the stability of most of the final output supplies. The second stages are also PWM converters but because their supply is the carefully controlled 12 volt intermediate voltage, they are tuned to run at the optimal 50/50 (flat out) conversion rate. Separate outputs with isolated grounds are provided for several loads. The various grounds are then connected to chassis at appropriate locations in order to minimize instrument noise. Eight analog voltage levels are included in the S/WAVES housekeeping stream.

Using the MIL-STD-1553 communications interface for spacecraft communications was an unfortunate choice which causes enormous fluctuations of the power services in synchronization with the spacecraft bus schedule. Despite considerable built-in capacitive support, the secondary voltages sag when the S/WAVES 1553 transceiver drives the bus (e.g. when S/WAVES telemetry is sent from the instrument to the spacecraft command and data handling system). Although the negative effects were minimized, it would be an improvement to avoid this noisy interface bus on future missions.

In sensitive scientific instruments of this kind, the power supply is an important element. The S/WAVES power supply achieved reasonable efficiency (70% end to end). The crystal controlled two stage design coupled with the isolation of outputs and grounds resulted in very good self compatibility within the S/WAVES instrument.

## 4.12 Resources, Mass, Power and Bits

The mass of the S/WAVES antenna assembly, including three monopole antennas, pream-plifier and mounting plate, was 7.080 kg. The electronics box, including all receivers, power supply and DPU had a mass of 5.750 kg. Including the harness and thermal blankets (for the antenna assembly), the total S/WAVES mass was 13.230 kg. S/WAVES has one nominal operating mode at turn-on and a wide variety of commandable options which do not affect instrument power consumption or bit-rate useage. The instrument has one spacecraft power interface which has a nominal primary load of about 15.4 W. The nominal allocation of spacecraft telemetry for S/WAVES is 2176 bits per second. This rate includes science data, instrument housekeeping, packet overhead and space weather data. Using a telecommand, it is possible to increase the actual bit-rate by as much as a factor of two.

# 5 Implementation/Integration

## 5.1 Accommodation on Spacecraft

The S/WAVES instrument, identical on the two STEREO spacecraft, was composed of two major pieces. The three mutually orthogonal antennas and preamplifier form one assembly and was attached to the rear face of the spacecraft, away from the sun (see Fig. 16). When deployed, the antennas extended into the sunlight. The S/WAVES receivers, power supply and data processing unit were assembled as a separate electronics box and was attached to the interior of the spacecraft structure. A cable harness connected the main electronics box to the preamplifier. S/WAVES had a single interface to the spacecraft power system and dual (for redundancy) 1553 interfaces to the spacecraft command and data handling system. Since, for safety reasons, the spacecraft was responsible for deploying the three antennas, each antenna had a simple filtered interface to the spacecraft deployment bus.



**Fig. 16** The S/WAVES antennas (indicated by *arrows*) as they appear on the anti-sunward side of the spacecraft
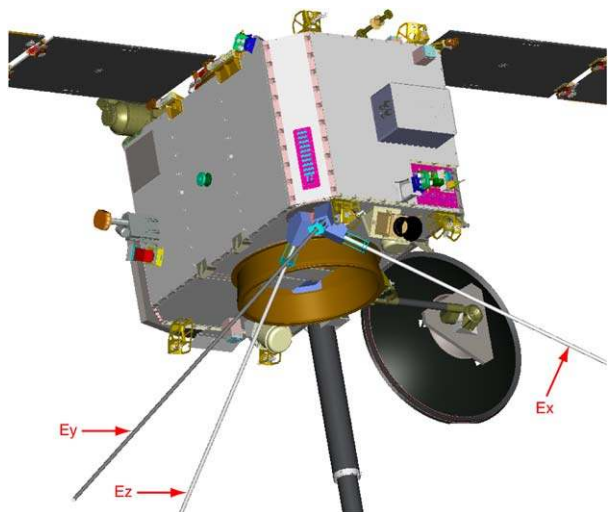
## 5.2 Electromagnetic Compatibility

Many of the S/WAVES scientific objectives are based on the measurement of low-level radio-frequency signals for which maximum sensitivity and minimum noise are required. S/WAVES measurement goals are to provide sensitivity at or below $\sim$7 nV/m/Hz$^{1/2}$. To make measurements of such small signal levels, several steps were implemented on STEREO. Efforts were made at the spacecraft, subsystem and instrument levels to produce observatories with minimal conducted and radiated electromagnetic interference. EMC tests were performed on each subsystem and instrument as part of its acceptance testing. A complete EMC survey was performed on each of the observatories before they were delivered to the launch site. As a result, the STEREO spacecraft were remarkably clean in ground tests and have proven acceptably clean on orbit.

Early in the Project, an EMC Board was formed to provide advice and direction in terms of electromagnetic compatibility. The NASA Project office, the spacecraft and the instrument teams all participated as members of the board's monthly meetings. In the beginning, the board laid out guidelines and requirements. The board provided advice on topics such as power supply design, shielding and grounding. The board held peer reviews of all detailed designs. As the subsystems and instruments completed their qualification and testing, the board reviewed EMC test results and suggested remedial action in cases thresholds were exceeded. The board also covered related areas such as electro-static cleanliness and magnetic cleanliness.

The following steps, which were implemented from the beginning of the project under the direction of the Project EMC Committee, produced excellent EMC results with a minimum investment in resources as well as minimum risk of problems in development or flight.

### 5.2.1 Electrostatic Shielding

The spacecraft body should form a Faraday cage to prevent stray electric field emissions from reaching the exterior and the S/WAVES antennas. Electronics boxes of spacecraft subsystems or instruments should also be well sealed. At points where instruments or harnesses penetrate from the interior to the exterior of the spacecraft structure, gaps must be sealed with conductive gaskets or tape.

### 5.2.2 Electrical Bonding

All electronics enclosures and especially those on the exterior of the spacecraft structure should be well grounded to the spacecraft structure. Electrical bonding should be maintained at all mechanical interfaces.

### 5.2.3 Grounding

Whenever possible, signal grounds should be connected to chassis grounds, in each electronics box. Primary power grounds must be isolated at all end users.

### 5.2.4 Harnessing

All harnesses should have an overall shield, connected to chassis ground at all ends. Within the bundles clock and other "noisy" signals must be shielded individually or in groups, with the shields connected to the signal ground at the source end or, when possible, at both ends of the cable. Primary power will be distributed as twisted shielded pairs or quads.

### 5.2.5 Frequency Control

The switching frequency of all DC/DC power converters must be stabilized at 50 kHz or harmonics thereof, with a preference for higher frequencies. Frequency control of at least one part in 10,000 is required and can be accomplished with synchronization or, as was done on STEREO, crystal controlled power supplies. Other major frequencies (clocks, oscillators, drive frequencies, etc.) used within the spacecraft should be recorded.

### 5.2.6 Solar Arrays

Capacitive filtering will be required for the leads from the solar array panels to the spacecraft power system in order to prevent noise from the power bus getting on to the panels.

### 5.2.7 Frequency Controlled Power Supplies: The Picket Fence Approach

One of the key approaches to this low-impact EMC plan is the use of frequency controlled power supplies throughout the spacecraft. In building electronic systems for use in space, it is recognized that some noise is unavoidable. DC to DC power converters usually require a chopping frequency and modern supplies using pulse width modulation produce switching transient noise at their conversion frequency and its harmonics. In recognition that some noise is inevitable, STEREO implemented a "picket fence" approach to power supplies and other sources of noise. All power converters were required to switch at 50 kHz or higher multiples. The frequency of conversion was also required to be very stable (typically using crystal control).

This combination results in a "picket fence" of noise at the power supply conversion frequencies and their harmonics (e.g., exactly 50 kHz, 100 kHz, 150 kHz and so on). As illustrated in Fig. 17, this picket fence of high order harmonics often extends across the entire S/WAVES band. Because the noisy frequencies are carefully controlled, the picket fence of noise has noise-free areas in the spectrum. The S/WAVES HFR receiver (described above) was built to take advantage of these noise free areas by making observations at odd multiples of 25 kHz (e.g., 125 kHz, 175 kHz, 225 kHz and so on across the spectrum) with a sharp comb filter. As a result, STEREO was not required to be very clean across the spectrum but only at odd multiples of 25 kHz. This approach, combining a safe design with a complete testing program made it possible to achieve S/WAVES scientific goals without an onerous EMC requirement or unverifiable testing limits.
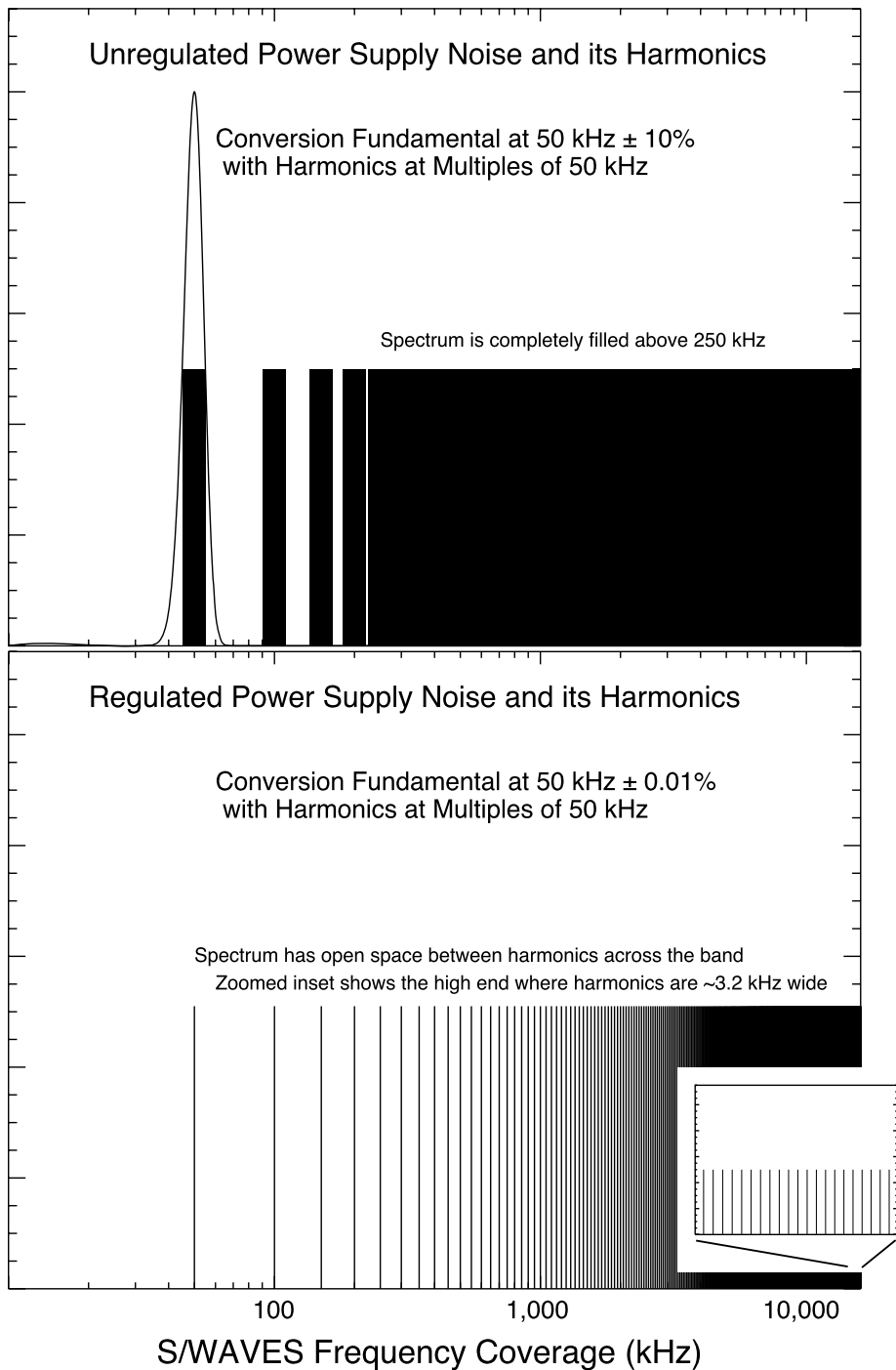
## 5.3 Inter-Instrument Communication

To help coordinate in-situ observations made on STEREO, the S/WAVES and IMPACT teams established an inter-instrument communication path. This path is implemented using the spacecraft 1553 communication bus, the bus also used for instrument telemetry and telecommand. Once each second a message passes from S/WAVES to IMPACT and another message goes from IMPACT to S/WAVES.

The quality of a TDS event is first determined with an arithmetic calculation by the DPU. The quality value that is assigned can be altered. Messages S/WAVES receives from IMPACT contain information about burst activity within the IMPACT instrument. Upon receiving news that IMPACT is observing substantial activity, corresponding S/WAVES TDS events can be amended to increase their quality score and ensure they are sent to the ground. This produces simultaneous S/WAVES and IMPACT burst events for correlative study.

S/WAVES can also use information in the message from IMPACT to trigger LRS bursts. The LRS sampling period is exactly half that of the IMPACT magnetometer, allowing direct comparison of low frequency wave activity with magnetic field activity.

Unregulated Power Supply Noise and its Harmonics

Conversion Fundamental at 50 kHz ± 10%
with Harmonics at Multiples of 50 kHz

Spectrum is completely filled above 250 kHz

Regulated Power Supply Noise and its Harmonics

Conversion Fundamental at 50 kHz ± 0.01%
with Harmonics at Multiples of 50 kHz

Spectrum has open space between harmonics across the band
Zoomed inset shows the high end where harmonics are ~3.2 kHz wide

100                 1,000             10,000

S/WAVES Frequency Coverage (kHz)

**Fig. 17** The "picket fence" made possible by strict control of power supply switching transients. The *top panel* shows an unregulated spectrum of power supply noise, covering the entire band above 200 kHz. The *bottom panel* shows the quiet gaps in the band made possible when power supplies have good frequency control

### 5.4 Calibrations

#### 5.4.1 Calibrations of the LFR, HFR and FFR

The calibrations for the LFR, HFR and FFR yield the receivers' responses and are used to convert binary telemetry data received on the ground into the physical parameters measured by the sensors. Complete calibrations were done in the laboratory before launch (ground calibrations) and are verified during the mission (in-flight calibration, described below).

*5.4.1.1 Ground Calibrations* Sophisticated and precise test equipment was designed and built for testing the instruments on the ground. Sine wave and white noise sources are provided. This test equipment is used for three kinds of test: gain curve measurements ("log law"), frequency bandwidth measurement and phase measurements.

For the receivers' gain curve measurements, a noise generator feeds a signal to the instrument through a variable programmable attenuator and a fixed attenuator. The programmable attenuator can step from 0 to 128 dB of attenuation with a programmable number of steps and step size. The response of the instrument is measured on all channels (1 for LFR band A, 2 for LFR bands B and C and the HFR). Channel 1 is connected to the antenna input $-Ex$ and channel 2 to $-Ez$. The input $-Ey$ is connected to the ground.

Figure 18 represents a typical gain curve obtained as a function of the attenuation for band A for the LFR. Nearly linear dependence between the input voltage and the continuous AGC output in telemetry points can be seen. For large signals (small attenuation) the AGC saturates, while for small signals, the receiver noise dominates.

This gain curve can be modeled by the following "log law" formula:

$$N = A_2 \cdot \log_{10}\left\{\left[10^{\frac{(A_1-x)}{10}} + 10^{\frac{A_4}{10}}\right]^{1/4} - 1\right\} + A_3,$$

where $N$ is the telemetry level (between 0 and 2047) and $x$ represents the attenuation of the input signal in dB. The parameters $A_1$, $A_2$, $A_3$ and $A_4$ have a physical significance in the AGC circuitry. They represent the receiver's gain, the offsets and the internal and external noise, respectively. These parameters are computed by numerical fitting and then used for the computation of physical data values. The red line on Fig. 18 represents the result of such a fit.

**Fig. 18** Typical analog output obtained as a function of attenuation in the case of LFR band A
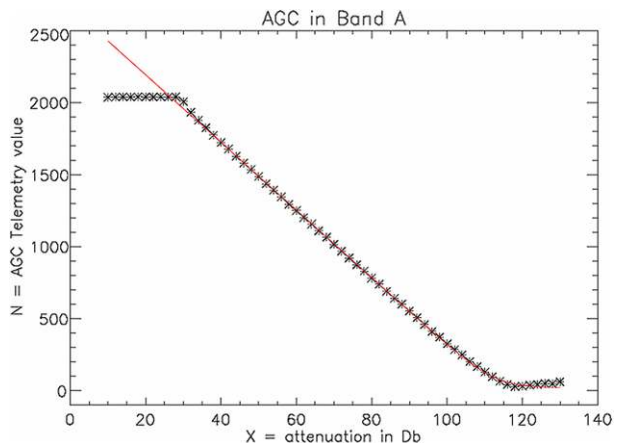
*5.4.1.2 In Flight Calibrations* For in flight verification of the instrument calibration, an internal noise generator provides eight attenuation levels (in 10 dB steps), applied successively to the receiver inputs at a point after the preamplifier. This calibration sequence allows a verification of the long-term stability of the receivers' gain and phase shift as functions of amplitude and frequency throughout the course of the mission. If a drift in gain is observed, the calibration parameters used in data analysis can be corrected. The calibration cycle is initiated by telecommand and will be performed at regular intervals (e.g., every 48 hours).

### 5.4.2 Inter Calibration between STEREO and Wind

During the early phases of the STEREO mission, the STEREO spacecraft are together in Earth orbit and, therefore, also near WIND, which has a very well calibrated radio receiver (WAVES) and accurate direction-finding capability. This provides a unique opportunity to inter-calibrate the STEREO radio receivers using WIND/WAVES as the calibration standard. Because of their high intensity and their particularly smooth, long-duration intensity profiles, solar type III bursts provide an excellent calibration source for all three spacecraft.

We have measured the maximum flux density for a number of type III radio bursts to establish the relationship between the flux measurements at WIND and STEREO. By providing an absolute calibration for the STEREO data, we can directly compare the profile of a type III burst at each spacecraft. Preliminary results of a comparison of a type III radio burst, derived using this inter-calibration procedure, are shown in Fig. 19. The type III profiles observed at STEREO A (red dots), STEREO B (green dots) and WIND/WAVES (blue dots) are seen to match very well. This inter-calibration technique will provide three identically calibrated spacecraft that will enable us to correctly interpret any differences in the radio burst profiles that may be observed when the STEREO spacecraft are well separated from each other and from WIND.

### 5.4.3 Calibration of the TDS

The various time domain systems (4 TDS channels and 8 LRS channels) were calibrated before launch by applying known sine waves to the preamplifier inputs. For the LRS (8 channels including the APM), the complex gains were also calculated from the circuit diagram.



**Fig. 19** The log of the radio flux density (in Solar Flux Units or sfu) of a type III radio burst observed simultaneously by STEREO A and B and by WIND/WAVES on December 7, 2006 at 425 kHz, as a function of the time in hours of the day
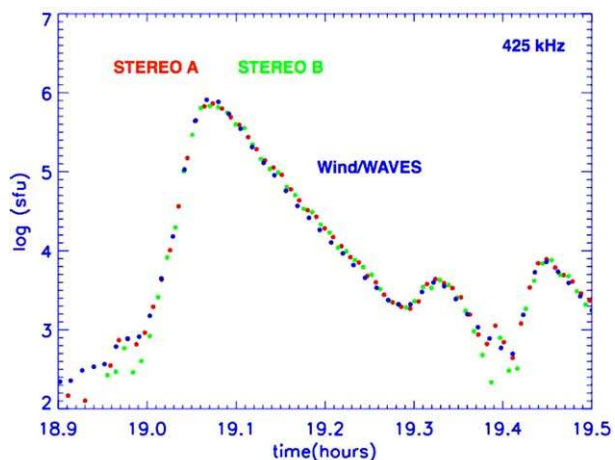
The magnitude of the calculated gains are shown as solid lines in Fig. 15 while the measured points are shown as discrete symbols. Knowledge of the complex gains is necessary to correct the sampled time sequences, which have been somewhat distorted by variations of gain with frequency, to give the true input waveform. The effects of the anti-aliasing filters have been included in the calibrations, and are shown in the figure.

### 5.4.4 Antenna Calibrations

The S/WAVES antenna reception properties have been analyzed by means of rheometry (electrolytic tank measurements) and numerical computer simulations (Bale et al. 2007; Macher 2005; Macher et al. 2006; Oswald et al. 2006a, 2006b; Rucker et al. 2005). The main focus is on the determination of the effective length vectors of the three antenna elements, since these are the quantities of interest for the evaluation of WAVES data (for wave direction finding and polarimetry). As an intermediate step, the simple antenna capacitances were measured as well.

A transfer matrix formalism (Macher 2005) was applied to take account of the coupling between the antennas, which is partly represented by the mutual capacitances. The aim was to determine the mentioned quantities for the quasi-static frequency range, where the wavelength is much greater than the antenna dimension. A frequency limit was sought below which the quasi-static parameters are applicable. For that purpose the frequency dependence of the effective length vectors over the whole frequency range of the S/WAVES receivers was calculated by wire-grid modeling. The obtained variation with frequency indicates that the sought limit is at about 1 MHz when the maximum achievable accuracy is required for each direction of wave incidence. The limit lies at about 2 MHz when it is sufficient to obtain this accuracy level on average over all directions of incidence. The details of these studies are described in Macher et al. (2006).

## 6 Scientific Operations

### 6.1 Space Weather forecasting with S/WAVES

The S/WAVES space weather beacon data (Biesecker et al. 2007) consists of receiver intensities from alternate channels of the HF band once per minute. This normally gives frequency resolution of 100 kHz from 125 kHz to 16 MHz, which corresponds to solar bursts occurring in the altitude range of 1–2 solar radii to as high as 80 solar radii. With this level of resolution in both time and frequency, solar bursts are easily detected, permitting estimates of the speed of CME-driven shocks and monitoring of the activity level associated with flares.

### 6.2 Archiving

#### 6.2.1 Data Archiving at the STEREO Science Center

The STEREO Science Center (SSC) at NASA Goddard Space Flight Center (see Eichstedt et al. 2007) is responsible for archiving the STEREO data during the life of the mission after which they will transfer the archives to the US National Space Science Data Center for permanent storage. For S/WAVES, the archive will include the level-0 telemetry files, the space weather beacon products (data and daily plots), and processed data such as daily summary plots, one-minute averages, tables of events, limited direction of arrival data, etc.

### 6.2.2 The Archiving at the CDPP Centre

The S/WAVES data are also archived at the CDPP (Centre de Données de Physique des Plasma). This archiving activity is a usual commitment when CNES (Centre National d'Etudes Spatiales, the French space agency) is contributing to a French hardware experiment. Calibrated power spectral data are archived in both full resolution and 1-minute averaged resolution. Daily summary plots are also available. The data is accessible through the CDPP web site (http://cdpp.cesr.fr).

### 6.3 Ancillary Radio Data

Several radio observatories will contribute ancillary data at frequencies higher than the upper frequency limit of S/WAVES, corresponding to radio phenomena in the lower levels of the solar corona and yielding information on the origin of particles and shock waves. In particular, the Nançay Radio Heliograph will bring support to both SECCHI and S/WAVES. Other instruments include the Nançay Decametric Array, the Gauribidanur Radio Heliograph in India, the BIRS radio spectrograph in Tasmania, the ARTEMIS spectrograph in Greece, and the Ondrejov spectrograph.

## 7 Education and Public Outreach

The S/WAVES team is committed to participating significantly in public outreach for the STEREO mission. The first outreach component will be an outreach web site, dedicated to making the S/WAVES data and results available to the public. The emphasis will be on a clear and interesting presentation for the scientifically oriented public. Appropriate links to the S/WAVES education site will be included. To convey the excitement of the scientific process, the S/WAVES data appear on the Web in a timely manner.

To promote the STEREO mission at science museums and similar locations, the S/WAVES team will participate in the development of one or more traveling exhibits, designed to explain STEREO and contributions to understanding the Sun-Earth Connection and space weather. Opportunities will be used in connection with the organization of the International Heliophysical Year 2007–2008, a celebration of the 50th anniversary of the International Geophysical Year in 1957–58, which was the starting point of space exploration and space physics.

The S/WAVES education plan and web presence will be based primarily on the triangulation and tracking of solar radio bursts from flares and CME-driven shocks. To this end, we are developing a number of components, to be made available on the web page http://swaves.gsfc.nasa.gov/, which explain the scientific background, the spacecraft instrumentation and data analysis techniques, and the grade level appropriate, hands on projects that one can do to understand S/WAVES science and data analysis. One of our themes will be the "invisible universe", because S/WAVES measures a section of the electromagnetic spectrum that is not visible to the human eye, but radio waves are a concept that people feel they understand. The ultimate web-based EPO component, towards which we are working, is user-oriented, interactive triangulation of radio bursts observed by S/WAVES, with radio-frequency correlated sonification. (Sonification makes good sense for radio waves, since they possess both frequency and intensity (volume). All that needs to be explained to the student/public is that we shift the radio frequencies to range of audible sound waves and, possibly, change the timescale.) Radio waves, radio receivers, and radio-stereoscopy provide a simple, understandable scientific perspective into the realm of space that we cannot "see".

In parallel with the data and web-based activities, we are developing several classroom-oriented, S/WAVES radio models. The simplest version is used to demonstrate the directionality of radio waves and how this permits triangulation of the sources. Two of these simple models can be built for a minimal sum. With these models, we can explain that:

– A simple spacecraft model with one monopole antenna demonstrates *directionality* of (AM) radio waves, and two models can convey triangulation *measurement concepts* (kindergarten–fourth grade).
– A spacecraft model with a triad antenna (3 orthogonal antennas, like the S/WAVES antennas) permits discussion of a realistic spacecraft system; measurement of angles leads to investigation of basic *geometry & trigonometry* (fifth–eighth grade).
– The triad antenna equations provide motivation for *spherical trigonometry* and more advanced *algebraic equation solving* (ninth–twelfth grade).

More sophisticated S/WAVES models are in development; they will use more advanced electronics to approximate the performance of a S/WAVES radio receiver system. With audio output or analog output to an oscilloscope, it will be easier for students and others to understand how S/WAVES works. Eventually, digital output to a computer could be examined and analyzed in a manner similar to data from the on-orbit S/WAVES data.

## 8 Summary and Conclusions

The S/WAVES investigation on the STEREO spacecraft has the following main scientific objectives:

– Remotely track and probe CME-driven shocks and flare electrons, at high frequency and time resolution, from their genesis in the low corona to their interaction with the terrestrial magnetosphere, thereby creating the link between the EUV and coronagraph images and the in-situ CME and particle observations.
– Measure in-situ the spatial extent and structure of CME-driven shocks and flare and CME-associated electron beams.
– Make remote and in-situ measurements of solar radio sources that may provide a deeper and more comprehensive understanding of the mechanisms that generate type II (CME) and type III (flare) radio bursts.
– Measure solar wind electron plasma density and temperature in regions of cold, dense plasma within CME-associated magnetic clouds using quasi-thermal noise methodologies.
– Study the role of plasma microphysics in CME-driven shocks.

To achieve these objectives the S/WAVES instrument consists of a set of radio receivers and analyzers covering the frequency range from a fraction of a hertz to 16 MHz plus a single frequency channel near 30 MHz.

The instrument is fully operational and meets its specifications on the two STEREO spacecraft on which the level of electromagnetic interference is generally lower than specified.

The stereoscopic radio technique will allow new studies of energetic particle phenomena associated with CMEs relevant to space weather studies. The S/WAVES measurements will be enhanced by similar investigations on the Ulysses, WIND, and Cassini spacecraft, and by an extensive support from ground-based observations at higher frequencies. The prospects are excellent to attain major progress for a comprehensive understanding of radio

phenomena associated with CMEs and active phenomena in the inner heliosphere leading, in particular, to a significant validation of radio diagnostics as a major tool for the prediction of the impact of solar activity in the heliosphere.

# References

M.H. Acuña et al., Space Sci. Rev. (2007, this issue). doi:10.1007/s11214-007-9259-2

M.J. Aschwanden, L.F. Burlaga, M.L. Kaiser et al., Space Sci. Rev. (2006). doi:10.1007/s11214-006-9027-8

S.D. Bale, P.J. Kellogg, D.E. Larson et al., Geophys. Res. Lett. **25**, 2929 (1998)

S.D. Bale, M.J. Reiner, J.-L. Bougeret et al., Geophys. Res. Lett. **26**(11), 1573 (1999)

S.D. Bale, P.J. Kellogg, F.S. Mozer, T.S. Horbury, H. Reme, Phys. Rev. Lett. **94**(21), 2150021 (2005)

S.D. Bale, R. Ullrich, K. Goetz et al., Space Sci. Rev. (2007, this issue). doi:10.1007/s11214-007-9251-x

D.A. Biesecker, D.F. Webb, O.C. St. Cyr, Space Sci. Rev. (2007, this issue). doi:10.1007/s11214-007-9165-7

J.-L. Bougeret, J. Fainberg, R.G. Stone, Astron. Astrophys. **141**, 17 (1984)

J.-L. Bougeret, M.L. Kaiser, P.J. Kellogg et al., Space Sci. Rev. **71**, 231 (1995)

J.-L. Bougeret, P. Zarka, C. Caroubalos et al., Geophys. Res. Lett. **25**, 2513 (1998)

G.E. Brueckner, R.A. Howard, M.J. Koomen et al., Sol. Phys. **162**, 357 (1995)

I.H. Cairns, J. Geophys. Res. **91**, 2975 (1986)

I.H. Cairns, J. Geophys. Res. **93**, 3958 (1988)

I.H. Cairns, M.L. Kaiser, in *The Review of Radio Science*: *1999–2002*, ed. by W.R. Stone (IEEE Press, 2002), p. 749

I.H. Cairns, S.A. Knock, in *Planetary Radio Emissions VI*, ed. by H. Rucker, W.S. Kurth, G. Mann (2006), p. 499

I.H. Cairns, P.A. Robinson, Geophys. Res. Lett. **24**, 369 (1997)

I.H. Cairns, P.A. Robinson, Astrophys. J. **509**, 471 (1998)

I.H. Cairns, P.A. Robinson, Phys. Rev. Lett. **82**(15), 3066 (1999)

H.V. Cane, R.G. Stone, J. Fainberg et al., Geophys. Res. Lett. **12**, 1285 (1981)

B. Cecconi, X. Bonnin, S. Hoang et al., Space Sci. Rev. (2007, this issue). doi:10.1007/s11214-007-9255-6

L.M. Celnikier, C.C. Harvey, R. Jegou, P. Moricet, M. Kemp, Astron. Astrophys. **126**(2), 293 (1983)

L.M. Celnikier, L. Muschietti, M.V. Goldman, Astron. Astrophys. **181**(1), 138 (1987)

G.A. Dulk, Y. Leblanc, J.-L. Bougeret, Geophys. Res. Lett. **26**, 2331 (1999)

J. Eichstedt, W.T. Thompson, O.C. St. Cyr, Space Sci. Rev. (2007, this issue). doi:10.1007/s11214-007-9249-4

R.E. Ergun, D. Larson, R.P. Lin et al., Astrophys. J. **503**, 435 (1998)

G.B. Field, Astrophys. J. **124**, 555 (1956)

V.L. Ginzberg, V.V. Zheleznyakov, Soviet Astron. **2**, 653 (1958)

N. Gopalswamy, S. Yashiro, M.L. Kaiser, R.A. Howard, J.-L. Bougeret, Astrophys. J. **548**, L91 (2001a)

N. Gopalswamy, A. Lara, S. Yashiro, M.L. Kaiser, R.A. Howard, J. Geophys. Res. **106**, 29207 (2001b)

N. Gopalswamy, S. Yashiro, G. Michalek et al., Astrophys. J. **572**, L103 (2002)

N. Gopalswamy, E. Aguilar-Rodriguez, S. Yashiro et al., J. Geophys. Res. **110**(A12) (2005). CiteID12S07

D.A. Gurnett, W.S. Kurth, D.L. Kirchner et al., Space Sci. Rev. **114**, 395 (2004)

R.A. Hess, R.J. MacDowall, J. Geophys. Res. **108**(A8) (2003). CiteID 1313

D.E. Hinkel-Lipsker, B.D. Fried, G.J. Morales, Phys. Fluids B **4**, 559 (1992)

S. Hoang, N. Meyer-Vernet, K. Issautier, M. Maksimovic, M. Moncuquet, Astron. Astrophys. **316**, 430 (1996)

S. Hoang, M. Poquerusse, J.-L. Bougeret, Sol. Phys. **172**, 307 (1997)

S. Hoang, M. Maksimovic, J.-L. Bougeret, M.J. Reiner, M.L. Kaiser, Geophys. Res. Lett. **25**(14), 2497 (1998)

Howard et al., SECCHI paper., Space Sci. Rev. (2008, this issue)

K. Issautier, N. Meyer-Vernet, M. Moncuquet, S. Hoang, J. Geophys. Res. **103**, 1969 (1998)

K. Issautier, N. Meyer-Vernet, M. Moncuquet, S. Hoang, D.J. McComas, J. Geophys. Res. **104**, 6691 (1999)

K. Issautier, M. Moncuquet, N. Meyer-Vernet, S. Hoang, R. Manning, Astrophys. Space Sci. **277**, 309 (2001a)

K. Issautier, R.M. Skoug, J.T. Gosling, S.P. Gary, D.J. McComas, J. Geophys. Res. **106**, 15665 (2001b)

P.J. Kellogg, Astron. Astrophys. **169**, 329 (1986)

P.J. Kellogg, Planet. Space Sci. **51**, 681 (2003)

P.J. Kellogg, N. Lin, *The 31st ESLAB Symposium, Correlated Phenomena at the Sun, the Heliosphere and in Geospace*, ed. by A. Wilson, SP-415 (ESTEC, Noordwijk, 1997)

P.J. Kellogg, D.A. Gurnett, G.B. Hospodarsky, W.S. Kurth, Geophys. Res. Lett. **28**, 87 (2001)

P.J. Kellogg, D.A. Gurnett, G.B. Hospodarsky et al., J. Geophys. Res. **108**(A1) (2003). CiteID 1045

P.J. Kellogg, S.D. Bale, F.S. Mozer, T.S. Horbury, H. Reme, Astrophys. J. **645**, 704 (2006)

S.A. Knock, I.H. Cairns, J. Geophys. Res. **10**(A1) (2005). CiteID A01101

D.E. Larson, R.P. Lin, J. Steinberg, Geophys. Res. Lett. **27**, 157 (2000)

Y. Leblanc, G.A. Dulk, J.-L. Bougeret, Sol. Phys. **183**, 165 (1998)

R.P. Lin, D.W. Potter, D.A. Gurnett, F.L. Scarf, Astrophys. J. **251**, 364 (1981)

N. Lin, P.J. Kellogg, R.J. MacDowall et al., Geophys. Res. Lett. **30**(19), 8029 (2003). doi:10.1029/2003GL017244

J.G. Luhmann, D.W. Curtis, P. Schroeder et al., Space Sci. Rev. (2007, this issue). doi:10.1007/s11214-007-9170-x

M. Maksimovic, S. Hoang, N. Meyer-Vernet et al., J. Geophys. Res. **100**(A10), 19881 (1995)

M. Maksimovic, J.-L. Bougeret, C. Perche et al., Geophys. Res. Lett. **25**(8), 1265 (1998)

W. Macher, Transfer matrix description of multi-port antennas and its application to the Mars Express/MARSIS radar. Doctoral Thesis, University of Technology, Graz, 2005

W. Macher, T.H. Oswald, H.O. Rucker, G. Fischer, STEREO-WAVES antennas: Reception properties in the quasi-static frequency range. Technical Report of the Space Research Institute of the Austrian Academy of Sciences, IWF-178, 2006

D.B. Melrose, Sol. Phys. **79**, 173 (1982)

N. Meyer-Vernet, C. Perche, J. Geophys. Res. **94**, 2405 (1989)

N. Meyer-Vernet, P. Couturier, S. Hoang, C. Perche, J.-L. Steinberg, Geophys. Res. Lett. **13**, 279 (1986)

N. Meyer-Vernet, P. Couturier, S. Hoang, C. Perche, J.-L. Steinberg, *AGU Monograph on Measurements Techniques in Space Plasmas*. Geophysical Monograph, vol. 103 (1998), p. 205

M. Moncuquet, N. Meyer-Vernet, S. Hoang, J. Geophys. Res. **100**, 21697 (1995)

T.H. Oswald, W. Macher, H.O. Rucker et al., Adv. Space Res. (2006a, submitted)

T.H. Oswald, W. Macher, G. Fischer et al., in *Planetary Radio Emissions VI*, ed. by H.O. Rucker, W.S. Kurth, G. Mann (Austrian Academy of Sciences Press, Vienna, 2006b), p. 475

A. Pedersen, Ann. Geophys. **13**, 118 (1995)

M. Poquerusse, S. Hoang, J.-L. Bougeret, M. Moncuquet, AIP Conf. Proc. **382**, 62 (1996)

M. Pulupa, S.D. Bale, American Geophysical Union, Fall Meeting 2006, abstract #SM13A-0349 (2006)

M.J. Reiner, M.L. Kaiser, Geophys. Res. Lett. **26**(3), 397 (1999)

M.J. Reiner, M.L. Kaiser, J. Fainberg, R.G. Stone, J. Geophys. Res. **103**, 29651 (1998a)

M.J. Reiner, M.L. Kaiser, J. Fainberg, J.-L. Bougeret, R.G. Stone, Geophys. Res. Lett. **25**, 2493 (1998b)

M.J. Reiner, M.L. Kaiser, J. Fainberg, R.G. Stone, J. Geophys. Res. **103**, 1923 (1998c)

M.J. Reiner, M. Karlicky, K. Jiricka et al., Astrophys. J. **530**, 1049 (2000)

M.J. Reiner, M.L. Kaiser, M. Karlicky, K. Jiricka, J.-L. Bougeret, Sol. Phys. **204**, 123 (2001a)

M.J. Reiner, M.L. Kaiser, J.-L. Bougeret, J. Geophys. Res. **106**, 29989 (2001b)

M.J. Reiner, B.V. Jackson, D.F. Webb et al., J. Geophys. Res. **100**(A9) (2005). CiteID 109S14

M.J. Reiner, J. Fainberg, M.L. Kaiser, J.-L. Bougeret, Sol. Phys. **241**(2), 351 (2007a)

M.J. Reiner, M.L. Kaiser, J.-L. Bougeret, Astrophys. J. **663**(2), 1369 (2007b)

P.A. Robinson, Sol. Phys. **139**, 147 (1992)

P.A. Robinson, I.H. Cairns, D.A. Gurnett, Astrophys. J. **407**, 790 (1993)

P.A. Robinson, Phys. Plasmas **2**, 1466 (1995)

P.A. Robinson, Rev. Mod. Phys. **69**, 507 (1997)

P.A. Robinson, I.H. Cairns, Sol. Phys. **181**, 363 (1998a)

P.A. Robinson, I.H. Cairns, Sol. Phys. **181**, 395 (1998b)

P.A. Robinson, I.H. Cairns, Phys. Plasmas **8**, 2394 (2001)

H.O. Rucker, W. Macher, G. Fischer et al., Adv. Space Res. **36**, 1530–1533 (2005)

C. Salem, J.-M. Bosqued, D.E. Larson et al., J. Geophys. Res. **106**, 21701 (2001)

K. Saito, A.J. Poland, R.H. Munro, Sol. Phys. **55**, 121 (1977)

R. Schwenn, A. Dal Lago, E. Huttumen, W.D. Gonzalez, Ann. Geophys. **23**, 1033 (2005)

J.-L. Steinberg, S. Hoang, A. Lecacheux, M.G. Aubier, G.A. Dulk, Astron. Astrophys. **140**, 39 (1984)

R.G. Stone, J.-L. Bougeret, J. Caldwell et al., Astron. Astrophys. Suppl. Ser. **92**, 291 (1992)

E.C. Stone, A.M. Frandsen, R.A. Mewaldt et al., Space Sci. Rev. **86**, 1 (1998)

G. Thejappa, R.J. MacDowall, Bull. Am. Astron. Soc. **37**, 1502 (2005)

T.W. Unti, M. Neugebauer, B.E. Golstein, Astrophys. J. **180**, 591 (1973)

A.J. Willes, I.H. Cairns, Publ. Astron. Soc. Aust. **18**, 355 (2001)

L. Yin, M. Ashour-Abdalla, R.L. Richard, L.A. Frank, W.R. Paterson, J. Geophys. Res. **104**, 12415 (1999)